OPEN ACCESS
Opin vísindi

This is not the published version of the article / Þetta er ekki útgefna útgáfa greinarinnar

Author(s)/Höf.:

Freysteinn Sigmundsson, Michelle Parks, Halldór Geirsson, Andrew Hooper, Vincent Drouin, Kristín S. Vogfjörd, Benedikt G. Ófeigsson, Sonja H. M. Greiner, Yilin Yang, Chiara Lanzi, Gregory P. De Pascale, Kristín Jónsdóttir, Sigrún Hreinsdóttir, Valentyn Tolpekin, Hildur María Friðriksdóttir, Páll Einarsson, Sara Barsotti

Title/Titill:

Fracturing and tectonic stress drives ultra-rapid magma flow into dikes

Year/Útgáfuár: 2024

Version/Útgáfa: Post-print, samþykkt ritrýnt handrit

Please cite the original version:
Vinsamlega vísið til útgefnu greinarinnar:

Sigmundson F. et al. (2024), Fracturing and tectonic stress drive ultrarapid magma flow into dikes, *Science*, *383*, Issue 6688, pp. 1228-1235, DOI: 10.1126/science.adn2838

Rights/Réttur: //

Title: Fracturing and tectonic stress drives ultra-rapid magma flow into dikes

Authors: Freysteinn Sigmundsson[1]*, Michelle Parks[2], Halldór Geirsson[1], Andrew Hooper[3], Vincent Drouin[2], Kristín S. Vogfjörd[2], Benedikt G. Ófeigsson[2], Sonja H. M. Greiner[1,4,5], Yilin Yang[1], Chiara Lanzi[1], Gregory P. De Pascale[1], Kristín Jónsdóttir[1], Sigrún Hreinsdóttir[6], Valentyn Tolpekin[7], Hildur María Friðriksdóttir[2], Páll Einarsson[1], Sara Barsotti[2]

Affiliations:
[1] Nordic Volcanological Center, Institute and Faculty of Earth Sciences, University of Iceland, Reykjavik, Iceland
[2] Icelandic Meteorological Office, Reykjavik, Iceland
[3] COMET, School of Earth and Environment, University of Leeds, Leeds, UK
[4] Department of Earth Sciences, Uppsala University, Uppsala, Sweden
[5] Center for Natural Hazard and Disaster Science (CNDS), Uppsala/Stockholm/Karlstad, Sweden
[6] GNS Science, Lower Hutt, New Zealand
[7] ICEYE OY, Maarintie 6, 02150 Espoo, Finland

Abstract: Many examples of exposed giant dike swarms can be found where lateral magma flow exceeded hundreds of kilometers. We show that massive magma flow into dikes can be established with only modest overpressure in a magma body, if a large enough pathway opens at its boundary, and gradual build-up of high tensile stress has occurred along the dike pathway prior to onset of diking. This explains rapid initial magma flow rates, modeled up to about 7400 m^3/s into a dike approximately 15-km-long, propagating under the town of Grindavík, SW-Iceland, in November 2023. Such high flow rates provide insight into the formation of major dikes and imply a serious hazard potential for high flow-rate intrusions that propagate to the surface and transition into eruptions.

One-Sentence Summary: A dike which formed beneath Grindavík Iceland in November 2023 shows how fracturing and tectonic stress can drive ultra-rapid magma flow into dikes.

Main Text: Stress has a major influence on the geometrical form and widening of dikes in the Earth's crust that are pathways for magma ascent. Uncertainties remain, however, on what governs the timescale of dike formation. In extensional tectonic settings, regional dikes are often vertical and aligned approximately perpendicular to the direction of the minimum compressive stress. In oblique spreading zones, a component of shearing on dikes is observed (*1*). At volcanic systems, stresses are also influenced by the local magmatic architecture. At divergent plate boundaries, tectonic stress is released by intruding dikes, fed by underlying magma sources, either from the mantle or within the crust. In some cases, the build-up of pressure in such sources can be inferred from geodetic measurements that reveal pre-diking inflation (*2*). The criterion for failure of magma bodies in the crust is uncertain; some models consider tensile failure and crustal tensile strength of about 1-10 MPa (*3*), whereas others assume shear failure by faulting that requires overpressure (pressure in excess of lithostatic pressure) in magma bodies with substantially higher values, on the order of tens of MPa (*4*). Thus, the level of overpressure in dike-feeding magma bodies is uncertain. Knowledge of these thresholds would enable better use of geodetic observations at volcanoes in forecasting future eruptions.

Because flow in subsurface magma channels in the crust is driven by pressure gradients, high overpressure in a source can explain high flow rates. However, if the tensile failure criterion is appropriate, it severely limits the overpressure that can form in a dike-feeding source. An alternative way to drive massive flow is if extensional processes have lowered the minimum compressional stress in the crust where the dike will form, and if the initial magma pathway emanating from a feeding magma source has a sufficiently large cross-sectional area. Our modelling of geodetic observations indicates this was the case when a ~15-km-long dike formed rapidly in November 2023 in the Svartsengi volcanic system on the Reykjanes Peninsula, Iceland, and partly propagated under the town of Grindavík, causing widespread damage and evacuation of the local population (Fig. 1).

The process of diking is associated with characteristic ground deformation and sometimes surface fracturing and faulting (1,*5-8*). These can be mapped and modeled to infer the shape and amount of opening in a dike. The location of a magma source feeding the dike may also be revealed through ground deflation. On 10 November 2023, a linear trend of migrating seismicity and associated ground deformation revealed a dike propagating rapidly from below the Sundhnúkur crater row on the Reykjanes Peninsula, passing under the town of Grindavík (referred to as the Grindavík dike) and extending under the ocean floor. This was concurrent with deflation of the nearby Svartsengi area, a central volcanic complex, which, along with an extensive fissure swarm forms the Svartsengi volcanic system (*9*). The area hosts a high-temperature geothermal field where the Blue Lagoon geothermal resort is located. The deflation occurred in an area where five inflation episodes occurred in the 2020-2023 period prior to the Grindavík dike (*10*, *11*, *12*). The events are a part of an ongoing period of volcano-tectonic activity on the Reykjanes Peninsula (*1*, *13*, *14*). The Grindavík dike continued to expand at low rates for days following its formation, and inflation began in the same area where co-diking deflation occurred when the dike formed. This inflation continued until 18 December 2023 when a diking event and fissure eruption occurred on the northern part of the Sundhnúkur crater row. The vigor of the eruption increased rapidly over a few hours, as eruptive fissures opened over a distance of ~4 km, then activity quickly declined, and the eruption ended 21 December after forming a ~3.5 km^2 lava flow. Following a similar increase in pressure over three weeks, another diking event and eruption occurred 14-16 January 2023 when lava flowed into the town of Grindavík.

For the Svartsengi area, studies of crustal seismic velocities are consistent with partially molten magma pockets or a magma reservoir. Seismic ambient-noise tomography

(*15*) infers an anomaly with low seismic velocities between 3 and 6 km depth at the location of the Svartsengi geothermal field, interpreted to be the heat source of the geothermal activity. Studies of the most recent eruptive products in the Svartsengi system from 1210-1240 C.E. infer a magma storage at 7-10 km depth (*16*). The Sundhnúkur crater row previously erupted ~2,350 years ago, when magma passed through an inferred zone of weakness (*17*). We analyze the Grindavík dike formation and the inflation and deflation of the Svartsengi area 27 October – 12 November, 2023 for a better understanding of the physical processes involved.

Geodetic and seismic observations and interpretation

Three-dimensional ground deformation is well resolved both temporally and spatially with dense Global Navigation Satellite System (GNSS) geodetic observations (figs. S1-S9) and interferometric analysis of synthetic aperture radar images (InSAR), using Sentinel-1, COSMO-SkyMed, and ICEYE satellites (figs. S10-S12). Seismicity recorded by the national seismic network of Iceland (SIL) operated by the Icelandic Meteorological Office shows the key features of events (Fig. 1, figs. S13-S16). Geodetic modelling was carried out (using data as explained below), assuming sources of deformation within a uniform elastic half space (*18*).

Seismicity increased dramatically in the Svartsengi area on 25 October 2023, followed by a new inflation period beginning on 27 October 2023 (figs. S4, S5). Geodetic modelling (*19*, *20*) (*18*) suggests a sill-shaped intrusive volume at ~5 km depth, with an average volume increase rate of ~7.5 m^3/s until 10 November 2023, when an accumulated volume of ~9×10^6 m^3 is inferred (Fig. 2). The depth estimate places the pressure increase near the local brittle-ductile boundary, based on depth distribution of seismicity and inferred plate boundary locking depth (*21*, *22*, *23*). Between January 2020 and May 2023, four inflation episodes have occurred in Svartsengi (fig. S2). Corresponding deformation data for these earlier events can also be explained with sill-shaped intrusions, with a total volume increase of (9–11)$\times10^6$ m^3 for the first three periods (*12*), and an additional volume of ~4×10^6 m^3 for the inflation period in May 2022 (figs. S17-S18). From 25 October to 9 November seismicity occurred with varying intensity in location and with time, extending from the Sundhnúkur crater row in the east, across Svartsengi geothermal area to Eldvörp crater row in the west, with additional more distant triggered earthquakes along the plate boundary (Fig. 1B). In the central part of the activity, several N-S strike slip earthquakes of magnitudes greater than M_W4 occurred on multiple faults. Throughout this time period seismicity beneath the Sundhnúkur crater row was most intense on the second day (26 October).

Around 7:00 UTC on 10 November 2023 rapid low-magnitude seismicity, typical of subsurface magma migration (*24*), started at 4-6 km depth under Sundhnúkur crater row, gradually moving 3.5 km northward to Stóra-Skógfell over the next 8.5 hours (Fig. 1C, figs. S13-S16). We did not detect surface deformation signals during this time. Southward migration of the seismicity commenced after a M_W4.1 event at 15:23; thereafter seismic propagation occurred both to the north and the south (Fig 1E). The propagation to the south was faster, and the events much larger than on the northern segment. At 16:56 a M_W4.8 earthquake occurred just north of Mt. Hagafell and more events immediately followed. At 18:01 a M_W5.2 event occurred at Hagafell, followed by a continuous swarm of small and large events that advanced at a fast pace towards Grindavík. By 18:30 the events had reached the town of Grindavík and by 19:30, earthquakes were detected south of the town. From just

before noon on 10 November until midnight, around 25 $M_W \geq 4$ earthquakes occurred, two of which were of M_W~5.2. At 16:40 UTC deformation commenced at high rates as detected by the GNSS network (Fig. 2, fig.S7). Horizontal and vertical deformation reached one meter by 20:00 UTC, after which deformation rates and seismicity decreased. The temporal evolution of GNSS displacements shows that the NE part of the dike expanded first followed by the SW part (fig. S6), in broad agreement with development of seismicity. Dike-induced extension was accommodated at the surface along dike-sub-parallel normal faults and fissures forming near Svartsengi and south to the coast including the town of Grindavík (fig. S19).

Geodetic modeling constrained by an interferogram utilizing a COSMO-SkyMed satellite image acquired 19:35 on 10 November, about 3 hours after the onset of surface movements, and GNSS displacements for the same period (Figs. 3-4, fig. S20) reveals that the dike volume at that time was already about ~$(70\text{-}80)\times10^6$ m^3. Further modeling incorporating line-of-sight offsets calculated from ICEYE, COSMO-SkyMed and Sentinel-1 synthetic aperture radar (SAR) satellite images, together with GNSS data, up until 19:00 on 12 November, indicate a dike volume of $(130\text{-}139)\times10^6$ m^3 (Fig. 4, fig. S21). The model has up to ~8 m opening at 2-4 km depth, as well as some strike-slip displacement. Deflation at Svartsengi in our model is best fit using a spherical point source (*11*) at depth of 4.0 to 4.2 km, with a volume decrease of $(76\text{-}82)\times10^6$ m^3 until 12 November.

We further modeled the temporal evolution of the dike opening using hourly GNSS displacements (*25*), allowing better derivation of the temporal evolution of the flow rate into the dike and the contraction volume of the subsidence source (Fig. 5, figs. S22-S25). The numbers derived from the modelling with GNSS data alone are scaled to give the same cumulative volume as inferred from GNSS and SAR data, as the hourly dike models derived using only GNSS data as the input have greater uncertainty. The maximum flow rate into the dike is inferred to be ~7400 m^3/s, between 18:00 and 19:00 on November 10.

Physical model

The deflation of the Svartsengi magma source 10-12 November amounts to ~80×10^6 m^3, whereas the cumulative inflation volume over the five inflow periods 2020-2023 period amounts to about ~23×10^6 m^3. GNSS measurements in the area back to 1993 (*22*) show no inflation episodes prior to 2020 (fig. S2). Since the time-scales of the November 2023 pre-diking inflation and co-diking deflation are days/weeks, we infer elastic response dominated during them, with pressure change scaling linearly with the amount of ground deformation. The volume ratio, ~23/80 = 0.29 gives a maximum value for the ratio of pre-eruptive pressure increase to co-eruptive pressure drop. If any relaxation of stress occurred between the inflation episodes prior to 10 November, then the ratio would be even lower. This calls for a physical model where the cumulative pre-diking pressure increase was modest, otherwise an unrealistically large co-diking underpressure (pressure less than ambient crustal pressure) would be inferred. The Kilauea 2018 caldera collapse occurred after a pressure drop of ~17 MPa (*26*), with a comparable value inferred at Bárðarbunga in 2014 (*27*), which can be taken as an upper bound on the observed underpressure required to trigger a caldera collapse in basaltic volcanic settings. No caldera collapse occurred in the events studied at Svartsengi, so we consider a pre-eruptive pressure increase substantially higher than 5 MPa at Svartsengi unlikely.

We test a physical model (Fig. 5) against observations and infer a set of approximate values of model parameters, including the amount of pressure increase and decrease in the

Svartsengi source, and the driving pressure needed for the rapid dike formation. We envision that during the Svartsengi inflation episodes, magma was emplaced into a crustal volume we refer to as a magma domain (*28*, *27*), which consists of liquid magma, partial melt, magma mush and hot solid rock (Fig. 5). This scenario is consistent with the five sill inflation models covering a similar area, within a zone of low-seismic velocities. We suggest the sills correspond to the top of the magma domain at ~5 km depth, that may be larger at deeper levels than the sills' area outline. Although models put the deflation source slightly shallower than the sill emplacement depth, we suggest the inferred sills mark the top of the magma domain that deflated. Fitting a point source to observed deformation, and assuming a uniform elastic halfspace, can cause model error that systematically influences depth estimates (*29*). The seismic velocity anomalies are several kilometers thick, although the actual value is uncertain.

For a fixed volume change, the pressure change in the magma domain depends on its shape and size, its compressibility, and the host rock shear modulus (*18*). A representative magma domain geometry is needed that does not produce unrealistically large underpressure during the deflation, and has a cross sectional area comparable to the pre-diking sills. We used a horizontal oblate spheroid, with horizontal semi-axes a = 4 km, b = 1.5 km, and c (the half-thickness of the magma domain) of 1.5 km. For these numbers and a crustal shear modulus of 10 GPa (*25*), the pressure drop associated with the inferred 10-12 November magma domain deflation volume (~80×10^6 m^3) is -21 MPa, and for the cumulative inflation volume prior to diking of (~23×10^6) m^3 it is 6 MPa. However, some of the pressure build-up associated with the inflation episodes may have been partly relaxed by viscoelastic or poro-viscoelastic relaxation (*30*, *31*, *32*). Observed deflation following previous Svartsengi inflations (Fig. S2) is consistent with this, and a more representative value for total pre-diking pressure increase in the magma domain due to inflow may be ~4-5 MPa, in line with the constraint from the absence of caldera collapse.

Buoyancy pressure at the top of the magma domain depends on the vertical extent of connected liquid magma, ΔH, and the density difference between magma and host rock, estimated at depth of 5-8 km to be 300 kg/m^3 (*27*). Assuming ΔH is in the range 1-3 km (considering magma lenses within the magma domain may not all be connected), then the buoyancy pressure is in the range 3-9 MPa. Assuming long-term stresses due to plate spreading and glacial isostatic adjustment are completely relaxed below the brittle-ductile boundary, the excess tensile stress on the boundary (hoop stress) is approximately equal to combined pressure increase due to magma inflow and buoyancy pressure (*27*), or ~(7-14) MPa. We consider this was the tensile strength, reached on 10 November. We interpret that magma flowed from the magma domain at ~5 km depth into the lower part of the central opening area of the dike and upwards to about 1.5-3 km depth where it spread more laterally (Fig. 4). This is the depth level of neutral buoyancy where basaltic magma has comparable density to the surrounding crust in Iceland (*27*, *33*). Increase in overpressure during upward migration depends on the average difference in density between host rock and magma, estimated here to be 200 kg/m^3 considering a smaller average difference in density at 2-5 km depth than at deeper levels (*27*). For 3-km of upward flow, the increase in overpressure is ~6 MPa, and the total overpressure ~(13-20) MPa, in the 'central zone of lateral divergence' in the upper part of the dike.

We consider further the effect of the tectonic stress. When a dike propagates, its opening will depend on the dike fluid pressure versus the host rock normal stress along the dike plane, both influenced by lithostatic pressure that cancels out. The remaining deviatoric normal stress acting on the dike as a result is primarily from tectonic stress. The excess

pressure in the dike is increased by the deviatoric normal stress. When the deviatoric stress is fullly relaxed, the excess pressure is reduced by the amount of a priori deviatoric normal stress (*33*). If a new patch of dike is opening at the far end of a propagating dike, then the amount of deviatoric normal stress there translates into a component of effective driving pressure for diking. The dilatational stress rate due to plate movement on the Reykjanes Peninsula is about is ~(0.009-0.011) MPa/yr near the plate boundary axis (*1*). Since 1240 C.E., when the last eruption took place, the amount of accumulated normal stress reduction on the dike plane may have amounted to ~(7-9) MPa. We take this as an estimate of the contribution to the driving stress. This adds to the inferred overpressure in the dike at 2 km depth, so the estimated driving pressure for magma flow is ~(20-29) MPa. This is the estimated maximum possible pressure drop in the magma domain; below this, the driving pressure would fall below zero and magma flow would stop.

The ratio of the dike volume and the contraction volume of the magma domain gives further constraints. For the 10-12 November dike and magma domain deflation, the inferred ratio is 1.6-1.8. This ratio depends on the shape of the magma domain, and the ratio between the shear modules of host rock and the compressibility of material within the magma domain (*34*, *35*, *36*). For the magma domain geometry and host rock shear modulus assumed above, and the volume ratio derived from our modelling, then the inferred compressibility of the magma domain is 0.06-0.08 GPa^{-1} (*18)*. The 1.6-1.8 volume ratio we find is at the lower end of ratios reported in earlier studies for basaltic systems (*34*, *36*), and the compressibility value is lower than an estimate for Icelandic basaltic magma (*27*). This is consistent with the magma domain not filled with liquid magma, but rather being a complex of hot solid host rock, liquid magma and magma mush.

The flow rate in a magma channel is proportional to the driving pressure (ΔP) and inversely proportional to the viscosity (η) of the magma and the length of the channel (L) (*37*). The flow rate furthermore scales with the cross-sectional area (A) of the channel and a geometrical factor (α) depending on the geometrical form of the channel and its minimum lateral dimension (*38*):

$$Q = \alpha \frac{A}{\eta L} \Delta P \qquad (1)$$

Here Q is the volumetric magma flow rate. The driving pressure for the flow depends on pressure conditions at the two ends of a channel. If the effective magma pathway from the magma body to the main dike has a rectangular cross-sectional area, $A=Dw$ where D is the long side and w is the short side length, then the geometrical factor in equation (1) is

$$\alpha_{rectangle} = \frac{w^2}{12} \qquad (2)$$

This equation was used to interpret magma flow in dikes formed in the Krafla rifting episode (*39*). For a driving pressure of (20-29) MPa, representative Icelandic basaltic magma viscosity in the range of 10-100 Pa s (*40*), flow path length of 5 km, then the flow rates we infer from geodetic modelling can be produced if the effective magma pathway has D in the

range 0.5-3 km and *w* in the range of 0.5-5 m (fig. S26). Such range of dike dimensions is commonly found in Iceland (*41*).

Widening of the narrowest part of the magma channel connecting the magma domain and the main dike body may control the rise time in magma flow towards a peak value. Our geodetic data suggest this was several hours (Fig. 5). As deflation continues the effect of the tectonic stress becomes proportionally larger in the driving pressure. The term related to overpressure due to pre-diking magma inflow disappears quickly and remaining contributions are due to buoyancy in the magma domain and the upward channel, as well as the tectonic stress. We infer that high tensile stress at the distal ends of a horizontally propagating dike is a key feature, as its important contribution to the driving pressure does not decay with time, as long as the dike propagates into an area where tensional stress has not been released.

The 18-21 December 2023 diking and eruption at the Sundhnúkar crater row was preceded by renewed magma inflow and pressure increase in the Svartsengi magma domain for five weeks. Following these events pressure gradually increased in the magma domain and diking and eruption occurred again on 14-16 January 2024. By modelling the temporal evolution of magma flow from co-diking GNSS observations as for the 10-12 November period, the inferred peak magma flow rate on 18 December is ~800 m^3/s, and ~1700 m^3/s on 14 January. The short-lived nature of the eruptions, and rapid decline of pressure in the feeding source during them, suggests limited overpressure in the feeding magma domain and rapid draining of magma from it, similarly to the November diking.

Implications

Our inferred peak magma flow rate of~7400 m^3/s is 2-3 orders of magnitude larger than in the 2021, 2022, and 2023 eruptions in the nearby Fagradalsfjall area (*1, 13, 14*). The flow rate is also larger than in the 2014-2015 Bárðarbunga events, when a total of ~2 km^3 of magma were emplaced partly in a 48 km long dike that formed over two weeks and partly erupted with an initial inferred magma flow rate of ~240 m^3/s (*42*). However, in the initial half of Krafla rifting episode 1975-1984, peak magma flow rates into dikes reached within a few hours of diking onset, were up to 2000-3000 m^3/s as estimated from continuous recording of ground tilt (*43*). The peak flow rate in the Grindavík dike is comparable to inferred average eruption rate in the first 12 days of the massive 1783-1784 Laki eruption when 14.7 km^3 erupted in total, during a 9-month period (*44*). Given sufficient supply, once most deviatoric stress is released along a laterally propagating dike, upward flow can result in an eruption with very high discharge rates. However, sustaining high driving pressure over a long duration of time (weeks or more), as occurred at Laki, requires either a much larger volume of magma in the feeding source than at Grindavík, slowing down the pressure drop as magma flows away from it, or caldera collapse, when sometimes large volumes of magma can be extracted into a laterally propagating dike at low pressure drop rates (*26, 42*). Furthermore, flow rates are highly dependent on the viscosity of the magma as well as its density (low density creating high buoyancy); inferences from the Northern Volcanic Zone of Iceland is that the majority of postglacial basaltic magma erupted had viscosity lower than 30 Pa s (*40*).

Our findings have implications for magmatic activity in other parts of the world where extensional processes gradually lower the minimum compressional stress in the crust, such as along the mid-oceanic ridges of the world, and Afar (East Africa) where incipient sea floor spreading takes place (*45*). The biggest volcano in the Cascades, the Newberry Caldera, has linear vent eruptions related to extension, and ample evidence for many non-erupting

intrusions (*46*). However, eruptions only occur around fractures that facilitate migration to the surface (*47*). Instability of volcano flanks can lead to extensional regimes. In Hawaii, the relationship between reduction in normal stress through volcano flank motion and timing of dike intrusions has been highlighted (*48*). Modest amounts of overpressure in the pre-diking/eruptive phase, combined with the development of underpressure in magma domains, with a range of volumes, plus potential for caldera formation, can explain the range of flow rates and volumes in diking and eruptions when the effects of tensile deviatoric stress are considered.

Some of the giant dike swarms on Earth (>300 km long) may have formed in association with the onset of large igneous provinces and continental break-up, in relation to mantle plumes impinging on the lithosphere, such as the Mackenzie dike swarm in Canada and the British Tertiary dike swarm (*49, 50*). Widespread uplift above an arriving mantle plume head creates tensile stress favorable for lateral diking radiating from a focal point, downslope off a plume-related topographic swell (*51*). The Grindavík 2023 dike shows how magma flow rates of over 7000 m^3/s into a dike can be established, when a sufficiently large fracture opens into a magma domain and the magma can flow into an area of high tensile stress. Long-distance lateral propagation is then facilitated if pressure in the magma domain drops slowly, which can be the case if the magma domain is very large, as expected at onset of large igneous provinces, or if a caldera collapse occurs (*26*, *42*). Other limiting factors for the length of lateral diking are the size of the area of tensional stress, which would be comparable to the size of plume heads prior to rifting above them, and solidification of the magma as it flows in a dike (*51*). Giant dikes may have formed over several weeks, with magma flow emanating from a localized magma domain at sustained magma flow rates comparable to that observed on 10 November 2023 in the Grindavík dike.

References and Notes

1. F. Sigmundsson, M. Parks, A. Hooper, H. Geirsson, K. S. Vogfjörd, V. Drouin, B. G. Ófeigsson, S. Hreinsdóttir, S. Hjaltadóttir, K. Jónsdóttir, P. Einarsson, S. Barsotti, J. Horálek, T. Ágústsdóttir, Deformation and seismicity decline before the 2021 Fagradalsfjall eruption. *Nature* **609**, 523–528 (2022).

2. E. Sturkell, P. Einarsson, F. Sigmundsson, H. Geirsson, H. Ólafsson, R. Pedersen, E. de Zeeuw-van Dalfsen, A. T. Linde, S. I. Sacks, R. Stefánsson, Volcano geodesy and magma dynamics in Iceland. *J. Volc. Geotherm. Res*. **150**, 14–34 (2006).

3. Jónsson, S., Tensile rock mass strength estimated using InSAR. *Geophys.Res. Lett.*, **39**, L21305 (2012)

4. G. Currenti, C. A. Williams, Numerical modeling of deformation and stress fields around a magma chamber: constraints on failure conditions and rheology. *Phys. Earth Planet. Inter*. **226**, 14–27 (2014).

5. A. M. Rubin, D. D. Pollard, Dike-induced faulting in rift zones of Iceland and Afar. *Geology* **16** (5), 413–417 (1988).

6. L. G. Mastin, D. D. Pollard, Surface deformation and shallow dike intrusion processes at Inyo Craters, Long Valley, California. *J. Geophys. Res.: Solid Earth* **93.**B11, 13221–13235 (1988).

7. J. S. Pallister, W. A. McCausland, S. Jónsson, Z. Lu, H. M. Zahran, S. El Hadidy, A. Aburukbah, I. C. F. Stewart, P. R. Lundgren, R. A. White, M. R. H. Moufti, Broad accommodation of rift-related extension recorded by dyke intrusion in Saudi Arabia. *Nat. Geosci*. **3**, 705–712 (2010).

8. F. Sigmundsson, M.Parks, R. Pedersen, K. Jónsdóttir, B. G. Ófeigsson, R. Grapenthin, S. Dumont, P. Einarsson, V. Drouin, E. R. Heimisson, Á. R. Hjartardóttir, M. Guðmundsson, H. Geirsson, S. Hreinsdóttir, E.

Sturkell, A. Hooper, Þ. Högnadóttir, K. Vogfjörð, T. Barnie, M. J. Roberts, “Magma Movements in Volcanic Plumbing Systems and their Associated Ground Deformation and Seismic Patterns” in *Volcanic and Igneous Plumbing Systems, Understanding Magma Transport, Storage, and Evolution in the Earth's Crust* (Elsevier, 2018).

9. K. Sæmundsson, M. Á Sigurgeirsson, G. Ó Friðleifsson, Geology and structure of the Reykjanes volcanic system, Iceland. *J. Volc. Geotherm. Res.* **391**, 106501 (2020).

10. H. Geirsson, M. Parks, K. Vogfjörd, P. Einarsson, F. Sigmundsson, K. Jónsdóttir, V. Drouin, B.G. Ófeigsson, S. Hreinsdóttir, C. Ducrocq, The 2020 volcano-tectonic unrest at Reykjanes Peninsula, Iceland: stress triggering and reactivation of several volcanic systems in *Proceedings of the EGU General Assembly 2021* (EGU 2021), EGU21–E7534.

11. Y. Cubuk-Sabuncu, K. Jónsdóttir, C. Caudron, T. Lecocq, M. M. Parks, H. Geirsson, A. Mordret, Temporal seismic velocity changes during the 2020 rapid inflation at Mt. Þorbjörn-Svartsengi, Iceland, using seismic ambient noise. *Geophys.Res. Lett.* ***48***, e2020GL092265 (2021).

12. Ó. G. Flóvenz, R. Wang, G. P. Hersir, T. Dahm, S. Hainzl, M. Vassileva, V. Drouin, S. Heimann, M. P. Isken, E. Á. Gudnason, K. Ágústsson, T. Ágústsdóttir, J. Horálek, T. R. Walter, E. Rivalta, Philippe Jousset, C. M. Krawxzyk, C. Milkereit, Cyclical geothermal unrest as a precursor to Iceland’s 2021 Fagradalsfjall eruption. *Nat. Geosci.* **15**, 397–404 (2022).

13. M. Parks, F. Sigmundsson, V. Drouin, Á. R. Hjartardóttir, H. Geirsson, A. Hooper, K. S. Vogfjörd, B. G. Ófeigsson, S. Hreinsdóttir, E. H. Jensen, P. Einarsson, S. Barsotti, H. M. Fridriksdóttir, Deformation, seismicity, and monitoring response preceding and during the 2022 Fagradalsfjall eruption, Iceland. *Bull. Volc*. **85**, 60 (2023).

14. H. Geirsson, M. Parks, C.Lanzi, Á. G. Birgisdóttir, V. Drouin, C. Ducrocq, F. Sigmundsson, B. Ófeigsson, P. Einarsson, K. Jónsdóttir, K. Vogfjörð, S. Hreinsdóttir, S. Greiner, in Proceedings of the 2023 AGU (AGU 2023), abstr. G41A–05

15. Martins, J. E., Weemstrab, C., Ruigrok, E., Verdela, A., Jousset, P., Hersir, G.P., 3D S-wave velocity imaging of Reykjanes Peninsula high-enthalpy geothermal fields with ambient-noise tomography, *J. Volc. Geotherm. Res*. **391**, 106685 (2020).

16. A. Caracciolo, E. Bali, S.A. Halldórsson, G.H. Guðfinnsson, M. Kahl, I. Þórðardóttir, G.L. Pálmadóttir, V. Silvestri, Magma plumbing architectures and timescales of magmatic processes during historical magmatism on the Reykjanes Peninsula, Iceland. *Earth Planet. Sci. Lett.* **621**, 118378 (2023).

17. M. H. Jenness, A. E Clifton, Controls on the geometry of a Holocene crater row: a field study from southwest Iceland. *Bull. Volc*. **71**, 715–728 (2009).

18. Materials and Methods, available as Supplementary Materials on Science Online.

19. Y. Okada, Surface deformation to shear and tensile faults in a half-space. *Bull. Seismol. Soc. Am*, ***75****, No. 4, 1135–1154 (*1985).

20. K. Mogi, Relations between the eruptions of various volcanoes and the deformations of the ground surface around them. *Bull. Earthquake Res. Inst. Univ. Tokyo*, **36**, 99–134. (1958).

21. H. Vadon, F. Sigmundsson, Crustal deformation from 1992 to 1995 at the Mid-Atlantic Ridge, southwest Iceland, mapped by satellite radar interferometry. *Science* **275**.5297, 194–197 (1997).

22. S. Hreinsdóttir, P. Einarsson, F. Sigmundsson, Crustal deformation at the oblique spreading Reykjanes Peninsula, SW Iceland: GPS measurements from 1993 to 1998. *J. Geophys. Res.: Solid Earth* **106**.B7, 13803–13816 (2001).

23. V. Drouin, F. Sigmundsson, Countrywide observations of plate spreading and glacial isostatic adjustment in Iceland inferred by sentinel-1 radar interferometry, 2015–2018. *Geophys. Res. Lett.* **46**.14, 8046–8055 (2019).

24. E. P. S. Eibl, C. Bean, K. S. Vogfjörd, Y. Ying, I. Lokmer, M. Möllhoff, F. Palsson, Tremor-rich shallow dyke formation followed by silent magma flow at Bárðarbunga in Iceland. *Nat. Geosci.*, **10**, 299–304 (2017).

25. Supplementary text, available as Supplementary Materials on Science Online.

26 K. Anderson et al., Magma reservoir failure and the onset of caldera collapse at Kīlauea Volcano in 2018. Science, **366**, 1214 (2019).

27. F. Sigmundsson, V. Pinel, R. Grapenthin, A. Hooper, S. A. Halldórsson, P. Einarsson, B. Ófeigsson, E. R. Heimisson, K. Jónsdóttir, M. T. Gudmundsson, K. Vogfjörd, M. Parks, S. Li, V. Drouin, H. Geirsson, S. Dumont, H. M. Fridriksdottir, G. B. Gudmundsson, T. J. Wright, T. Yamasaki, Unexpected large eruptions from buoyant magma bodies within viscoelastic crust. *Nat. Comm.* **11**, 2403 (2020).

28. F. Sigmundsson, New insights into magma plumbing along rift systems from detailed observations of eruptive behavior at Axial volcano. *Geophys. Res. Lett*. **43**, 12,423–12,427 (2016).

29. R. Foroozan, D. Elsworth, B. Voight, G. S. Mattioli, Dual reservoir structure at Soufrière Hills Volcano inferred from continuous GPS observations and heterogeneous elastic modeling. *Geophys. Res. Letters* **37**.19 (2010).

30. T. Yamasaki, T. Kobayashi, T. J. Wright, Y. Fukahata, Viscoelastic crustal deformation by magmatic intrusion: a case study in the Kutcharo caldera, eastern Hokkaido, Japan. *J. Volcanol. Geotherm. Res*. **349**, 128–145 (2018).

31. Y. Liao, S. A. Soule, M. Jones, H. Le Mével, The mechanical response of a magma chamber with poroviscoelastic crystal mush. *J. Geophys. Res. Solid Earth*, **126**(4), e2020JB019395 (2021).

32. R. Alshembari, J. Hickey, B. J. Williamson, K. Cashman, Unveiling the rheological control of magmatic systems on volcano deformation: The interplay of poroviscoelastic magma-mush and thermo-viscoelastic crust. *J. Geophys. Res. Solid Earth*, **128**(7), e2023JB026625 (2023).

33. E. R. Heimisson, A. Hooper, F. Sigmundsson, Forecasting the path of a laterally propagating dike. *J. Geophys. Res. Solid Earth*, **120**, (2015).

34. E. Rivalta, P. Segall (2008), Magma compressibility and the missing source for some dike intrusions, *Geophys. Res. Lett*., **35**, L04306 (2008)

35. K. Anderson, K., and P. Segall, Physics-based models of ground deformation and extrusion rate at effusively erupting volcanoes, *J. Geophys. Res*. **116**, B07204, (2011).

36. S. Hreinsdóttir, F. Sigmundsson, M. J. Roberts, R. Grapenthin, P. Arason, T. Árnadóttir, J. Hólmjárn, R. A. Bennet, M. T. Gudmundsson, B. Oddsson, B. G. Ófeigsson, T. Villemin, T. Jónsson, E. Sturkell, Á. Höskuldsson, G. Larsen, T. Thordarson, B. A. Óladóttir, Volcanic plume height correlated with magma pressure change at Grímsvötn Volcano, Iceland. *Nat. Geosci.* **7**, 214–218 (2014).

37. C. Jaupart, "Magma ascent at shallow levels" in *Encyclopedia of Volcanoes* (Academic Press, 2000), pp. 237–245.

38. F. Sigmundsson, "Recent basaltic eruptions in Iceland and the dynamics of co-eruptive subsurface magma flow" in *Forecasting and Planning for Volcanic Hazards, Risks and Disasters, Vol. 2 in Hazards and Disasters Series* (Elsevier, 2021), pp. 413–438.

39. P. Einarsson, B. Brandsdottir, Seismological evidence for lateral magma intrusion during the July 1978 deflation of the Krafla volcano in NE-Iceland. *J. Geophys*. **47**, 160–165 (1980).

40. M. Hartley M and J. Maclennan, Magmatic densities control erupted volumes in Icelandic volcanic systems. *Front. Earth Sci.*, **6**:29. doi: 10.3389/feart.2018.00029 (2018)

41. A. Gudmundsson, "The geometry and growth of dykes" in *Physics and Chemistry of dykes* (Balkema, 1995), pp. 23–34.

42. M. T. Gudmundson, K. Jónsdóttir, A. Hooper, E. P. Holohan, S. A. Halldórsson, B. G. Ófeigsson, S. Cesca, K. S. Vogfjörd, F. Sigmundsson, T. Högnadóttir, P. Einarsson, O. Sigmarsson, A. H. Jarosch, K. Jónasson, E. Magnússon, S. Hreinsdóttir, M. Bagnardi, M. M. Parks, V. Hjörleifsdóttir, F. Pálsson, T. R. Walter, M. P. J. Schöpfer, S. Heimann, H. I. Reynolds, S. Dumont, E. Bali, G. H. Gudfinnsson, T. Dahm, M. J. Roberts, M. Hensch, J. M. C. Belart, K. Spaans, S. Jakobsson, G. B. Gudmundsson, H. M. Fridriksdóttir, V. Drouin, T. Dürig, G. Aðalgeirsdóttir, M. S. Riishuus, G. B. M. Pedersen, T. van Boeckel, Björn Oddsson, M. A. Pfeffer, S. Barsotti, Gradual caldera collapse at Bárdarbunga volcano, Iceland, regulated by lateral magma outflow. *Science* **353,** aaf8988 (2016).

43. E. Tryggvason, Subsidence events in the Krafla area, North Iceland, 1975–1979. *J. Geophys*. **47**, 141–153 (1980).

44. Th. Thordarson, S. Self, Atmospheric and environmental effects of the 1783–1784 Laki eruption: A review and reassessment. *J. Geophys. Res*. **108** (D1), 4011 (2003).

45. T. Wright, T., F. Sigmundsson, F., C. Pagli, *et al.*, Geophysical constraints on the dynamics of spreading centres from rifting episodes on land. *Nature Geosci* **5**, 242–250 (2012).

46. M. W. Beachly, E. E. E. Hooft, D. R. Toomey, G. P. Waite, Upper crustal structure of Newberry Volcano from P-wave tomography and finite difference waveform modeling, *J. Geophys. Res.* **117**, B10311 (2012).

47. D. Mckay, J. Donnelly Nolan, R. Jensen, and D. Champion (2009), The post-Mazama northwest rift zone eruption at Newberry Volcano, Oregon, in *Volcanoes to Vineyards: Geologic Field Trips Through the Dynamic Landscape of the Pacific Northwest, Field Guide*, vol. **15**, edited by J. E. O'Connor et al., pp. 91–110, Geol. Soc. of Am., Boulder, Colo., doi:10.1130/2009.fld015(05) (2009).

48. E. K. Montgomery-Brown, A. Miklius, Periodic dike intrusions at Kīlauea volcano, Hawai'i. *Geology*, **49**(4), 397-401 (2021).

49. R. E. Ernst, J. W. Head, E. Parfitt, E. Grosfils, L. Wilson, Giant radiating dike swarms on Earth and Venus, *Earth Sci. Rev.* **39**, 1–58 (1995).

50. R. E. Ernst, E. B. Grosfils, D. Mege, Giant dike swarms: Earth, Venus, and Mars. *Ann. Rev. Earth and Plan. Sci.*, ***29***(1), 489–534 (2001).

51. Y. A. Fialko, A. M. Rubin, Thermal and mechanical aspects of magma emplacement in giant dike swarms. *J. Geophys. Res.: Solid Earth*, ***104***(B10), 23033-23049 (1999).

52. A. E. Clifton, S. A. Kattenhorn, Structural architecture of a highly oblique divergent plate boundary segment. *Tectonophysics*, **419**, 27–40 (2006).

53. G. Pedersen, J. M.C. Belart, B. Óskarsson, M. Gudmundsson, G. N. Högnadóttir, Á. T. Hjartardóttir, V. Pinel, E. Berthier, T. Dürig, H. Reynolds, C. Hamilton, G. Valsson, P. Einarsson, D. Ben-Yehoshua, A. Gunnarsson, B. Oddsson, Volume, Effusion rate, and lava transport during the 2021 Fagradalsfjall eruption: results from near real-time photogrammetric monitoring. *Geophys. Res. Lett*. **49**, e2021GL097125 (2022).

54. S. R. Gunnarson, J. M. C. Belart, B. V. Óskarsson, M. T. Gudmundsson, Th. Högnadóttir, G. B. M. Pedersen, T. Dürig, V. Pinel, Automated processing of aerial imagery for geohazards monitoring: Results from Fagradalsfjall eruption, SW Iceland, August 2022 (1.0) [Data set]. Zenodo. (2023); https://doi.org/10.5281/zenodo.7701194.

55. H. Jóhannesson, K. Sæmundsson Jarðfræðikort af Íslandi 1: 600 000, höggun: Geological map of Iceland 1: 600 000–Tectonics. Icelandic Institute of Natural History, Reykjavík (2009).

56. H. Jóhannesson, K. Saemundsson, Geological Map of Iceland–Tectonics, 1:500,000. Icelandic Institute of Natural History, Reykjavík (1998).

57. LMI (2022). Landmælingar Íslands. Available at: https://www.lmi.is/is/um-lmi/frettayfirlit/ny-uppfaersla-a-haedarlikani-af-islandi.

58. D. F. Argus, R. G. Gordon, C. DeMets, Geologically current motion of 56 plates relative to the no-net-rotation reference frame. *Geochem. Geophys. Geosyst*. **12**, 11 (2011).

Acknowledgments: We thank two anonymous reviewers and the editor for comments that greatly helped to greatly improve the manuscript, and Ásta Rut Hjartardóttir for help making Fig. 1. We thank the Institute of Geophysics, Czech Academy of Sciences, and the Iceland GeoSurvey for allowing access to data acquired from seven of their seismic stations (currently running under the NASPMON project (Reykjanet (2022)) connected to monitoring system of the Icelandic Meteorological Office (IMO), to improve the detection and routine locations of earthquakes and the use of data from three of these stations (lag, lfe, iss) in the relative relocations of seismicity along the dike. The NASPMON project (Natural Seismicity as a Prospecting and MONitoring tool for geothermal energy extraction) benefits from a grant from Iceland, Liechtenstein, and Norway through the EEA Grants and the Technology Agency of the Czech Republic within the KAPPA Programme. We thank the IMO and University of Iceland technicians for support and operation of the GNSS and seismic stations. The diligence and support from the Natural Hazards Specialists (on duty in the IMO monitoring room) and IMO's seismic analysts is greatly appreciated. We also thank participants of various science and evaluation meetings held in connection to the Reykjanes unrest, and the National Commissioner of the Icelandic Police and their Department of Civil Protection. The Geohazard Supersites and Natural Laboratory (GSNL) Icelandic Volcanoes Supersite project supported by the Committee on Earth Observing Satellites is acknowledged for providing access to satellite data that was utilized in this study. We thank the GEO-GSNL initiative for their ongoing support of InSAR monitoring/research in Iceland. COMET is the UK NERC Centre for the Observation and Modelling of Earthquakes, Volcanoes and Tectonics.

Funding: This research was supported by the Icelandic Research Fund (grant numbers 228933-051 and 239615-051), the University of Iceland Research Fund, and the H2020 DEEPVOLC project funded by the European Research Council (grant number 866085), and the ChEESE-2P Horizon 2021 EuroHPC JU-RIA project (GA No. 101093038)..

Author contributions: F.S. coordinated the writing of the paper and the development of the ideas presented, together with M.P. Geodetic modelling and interpretation was carried out A.H, M.P., V.D. and C.L. GNSS observations and analysis were carried out by H.G., B.G.Ó., S. H., Y.Y. and H.M.F.. InSAR analysis were carried out by V.D. and V.T.. Seismic analysis was done by K.S.V., supported by K. J.. G.P.D.P. led analysis of graben formation. S.B. led the evaluation of the implications of the study for volcanic hazards. All the authors contributed to evaluation of the modelling, discussion of the results and the writing of the paper. S.H.M.G. created Fig. 5c; S.H.M.G., Y.Y. and C.L. compiled Fig. 1, 2 and 3.

Competing interests: None.

Data and materials availability: All data will be made available in an open access repository.

Supplementary Materials

One pdf file

Fig. 1. Location map and seismicity. **(A)** Western part of the Reykjanes Peninsula showing the Svartsengi, Reykjanes (R) and Fagradalsfjall (F) volcanic systems, fractures (*52*), Fagradalsfjall lavas (*53, 54*), fissure swarms (*55*), lava fields from previous eruptive period (*56*), plate boundary axis (*1*), and background digital elevation model (*57*). Inlet: Iceland with fissure swarms (yellow areas) central volcanoes (dashed ovals) and far field spreading direction (*58*). Reykjanes Peninsula is marked by the black rectangle. **(B)** Reviewed seismicity from the VI/SIL data base during the inflation period, 27 October – 9 November, colored according to time of occurrence showing the ~ 3 km wide band of seismicity following the trend of the plate boundary. The projection of the dike emplaced on 10 November is shown by dashed line and the red segment indicates the area of largest widening. **(C)** Seismicity from 00:00-15:00 on 10 November. **(D)** Dike seismicity from 15:01 on 10 November to 12:00 on 11 November, showing the full extent of the dike and seismicity in the Svartsengi area. Events mentioned in the text are identified on the plot. Star marked magnitudes are from the GFZ GEOFON moment tensor solutions. **(E)** Time evolution of seismicity with latitude showing propagation to north and south on 10 November. Seismicity before 15:00 on the 10th is shown in blue and thereafter in red. The last vertical hatched grey line marks midnight on the 10 November. As only a fraction of the seismicity has been reviewed, the events appear to be episodic, with gaps in between, although the activity was continuous through the whole period.

Fig. 2. Inflation of Svartsengi, 27 October – 10 November. **(A)** GNSS displacements, observed and modeled. The triangles show the locations of GNSS stations used in the geodetic modelling. The rectangle indicates the surface projection of the modelled sill that best fits observations **(B)** Line-of-Sight (LOS) displacement of unwrapped COSMO-SkyMed interferogram. Arrows indicate the heading (long arrow) and look direction (short arrow) of COSMO-SkyMed satellite acquisition **(C)**. Predicted LOS displacement. **(D)** Residuals (the difference between observations (B) and model predictions (C)).

Fig. 3. Geodetic observations of the dike formation. (**A**) Displacement and cumulative displacement time series from GNSS station SENG (labelled in panel B). **(B)** GNSS displacements, observed and modeled. The shaded background shows topography, and the thin lines indicate roads. The triangles show the locations of GNSS stations used in the geodetic modelling. (**C**) ICEYE interferogram 10-11 November at 11:44, with the long arrow indicating the flight direction and the short arrow the line-of-sight direction. Each color fringe represents 15.5 mm of relative line-of-sight displacement. **(D)** Line-of-sight pixel offsets estimated from same images as (C). **(E)** Vertical displacements estimated from ICEYE, COSMO SkyMed and Sentinel-1 pixel offset data. More data spanning the dike formation are shown in Fig. S11.

Fig. 4. Geodetic models of dike formation, 10 – 12 November. (A) Median values of dike opening in a model until 19:35 on 10 November **(B).** Same as A, until 19:00 on 12 November. High-precision relocated seismicity related to the dike is overlain on the model,

showing the maximum depth of seismicity matching the depth of the dike intrusion and the slightly shallower maximum depth in the area of maximum widening. The surface projection of the dike is shown in Fig. 3B.

Fig. 5. Magma flow rates and schematic model. **(A)** Inferred volume change rate and **(B)** cumulative volume of the Grindavík dike and the magma domain centered under Svartsengi, based on modelling of GNSS data (*25*). **(C)** Illustration of the Grindavík dike and the proposed magma domain under Svartsengi. The magma domain underlies the plate boundary axis (outlined by North-South striking strike-slip faults) and reaches approximately from the Eldvörp crater row in the west until close to Mt. Hagafell in the east. The Grindavík dike propagated under the NE-SW striking Sundhnúkur crater row in the north and under the town of Grindavík in the south, where a graben formed on 10 November (black lines). Surface projections of the Grindavík dike and the crustal cross section are outlined by red dashed and grey solid lines on the surface, respectively. Illustration is not to scale.

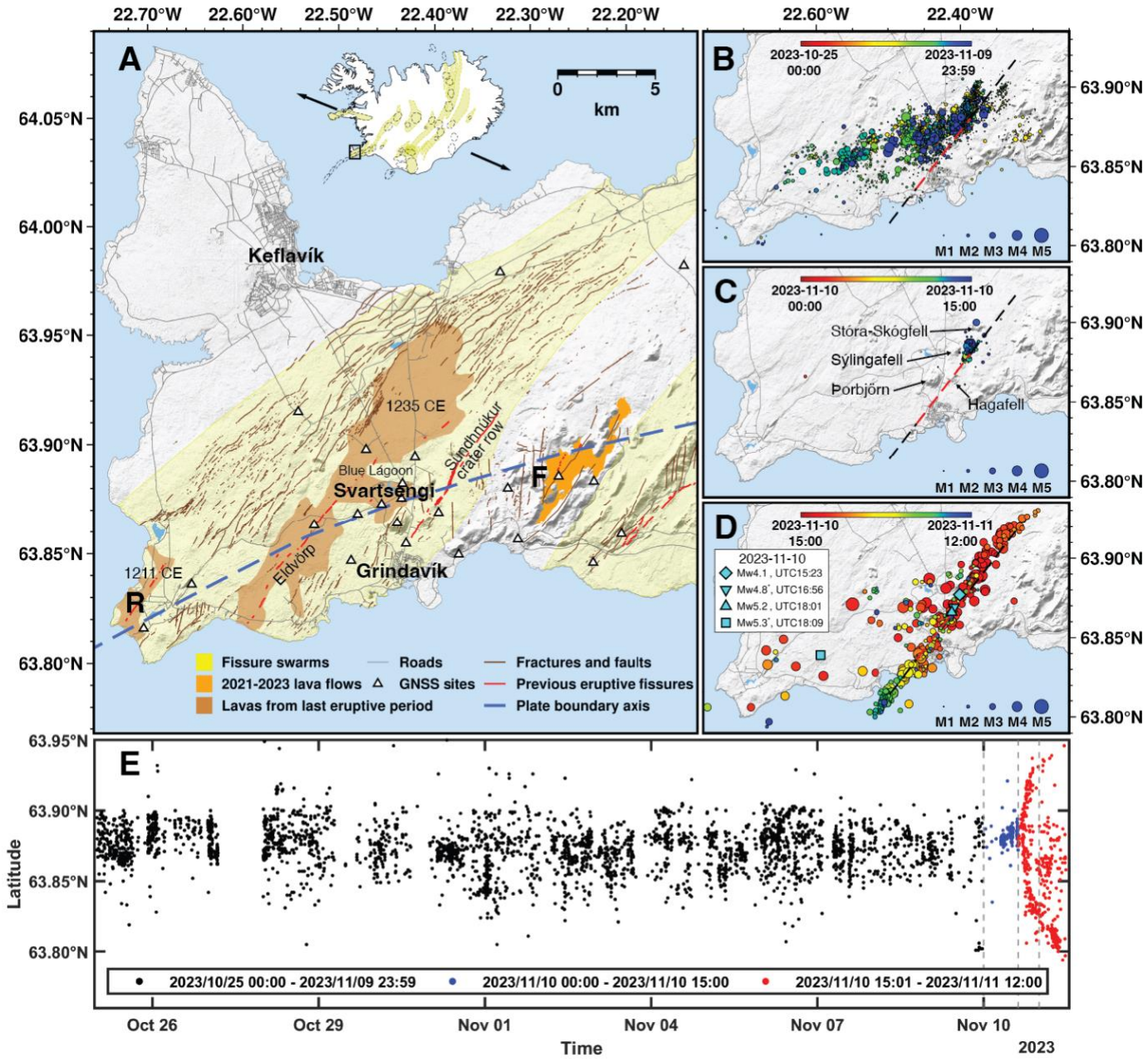
A
B
C
D
E
Keflavík
Grindavík
Svartsengi
Blue Lagoon
1235 CE
1211 CE
Sundhnúkur crater row
Eldvörp
R
F
0
5
km
Fissure swarms
2021-2023 lava flows
Lavas from last eruptive period
Roads
GNSS sites
Fractures and faults
Previous eruptive fissures
Plate boundary axis
2023-10-25 00:00
2023-11-09 23:59
2023-11-10 00:00
2023-11-10 15:00
2023-11-11 12:00
Stóra-Skógfell
Sýlingafell
Þorbjörn
Hagafell
M1 M2 M3 M4 M5
2023-11-10
Mw4.1 , UTC15:23
Mw4.8 , UTC16:56
Mw5.2 , UTC18:01
Mw5.3 , UTC18:09
Latitude
Time
2023/10/25 00:00 - 2023/11/09 23:59
2023/11/10 00:00 - 2023/11/10 15:00
2023/11/10 15:01 - 2023/11/11 12:00
Oct 26
Oct 29
Nov 01
Nov 04
Nov 07
Nov 10
2023

Fig. 1

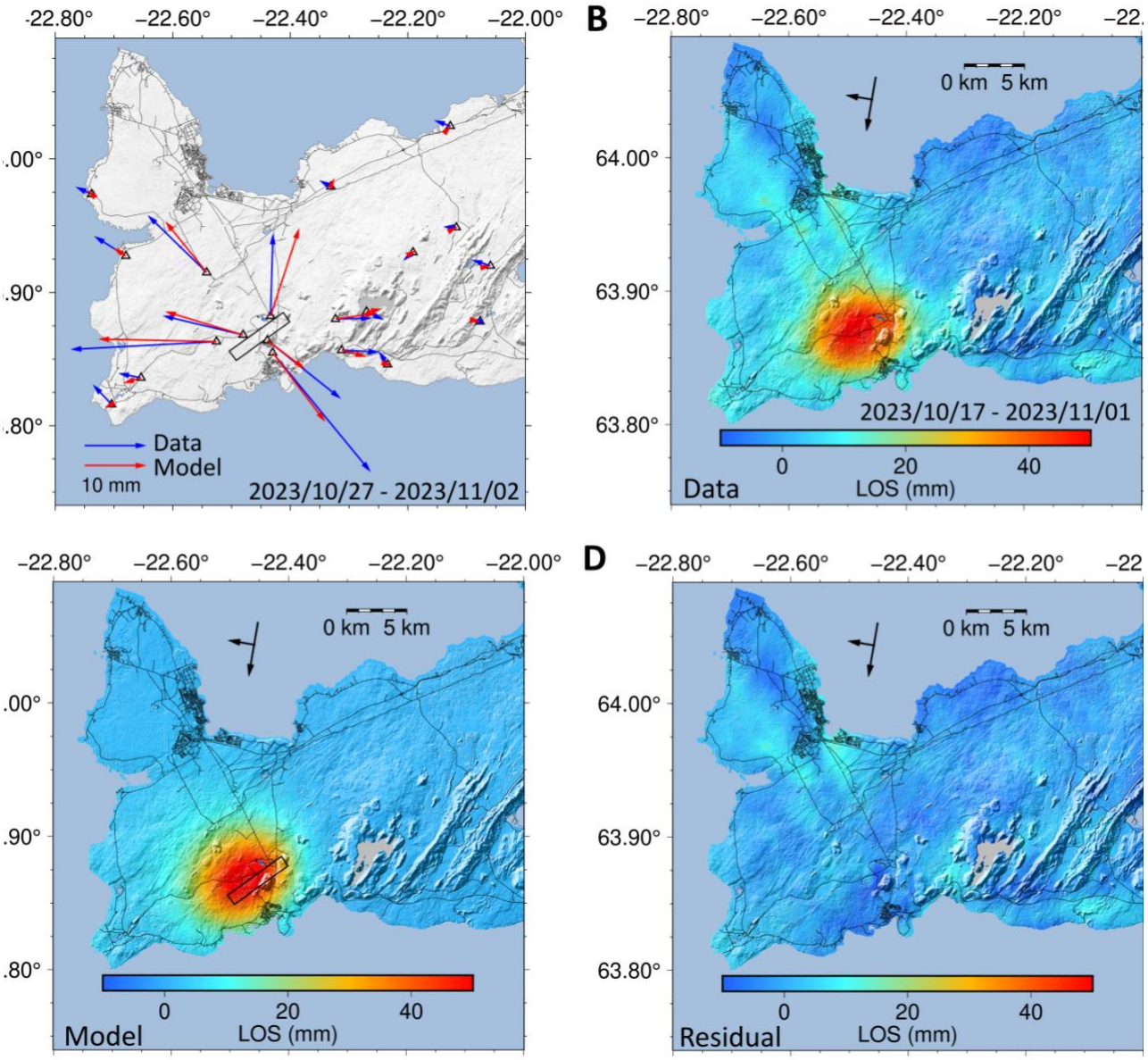
-22.80°
−22.60°
−22.40°
−22.20°
−22.00°
.00°
.90°
.80°
Data
Model
10 mm
2023/10/27 - 2023/11/02
B
−22.80°
−22.60°
−22.40°
−22.20°
64.00°
63.90°
63.80°
0 km 5 km
2023/10/17 - 2023/11/01
0
20
40
Data
LOS (mm)
−22.80°
−22.60°
−22.40°
−22.20°
−22.00°
.00°
.90°
.80°
0 km 5 km
0
20
40
Model
LOS (mm)
D
−22.80°
−22.60°
−22.40°
−22.20°
64.00°
63.90°
63.80°
0 km 5 km
0
20
40
Residual
LOS (mm)

Fig. 2

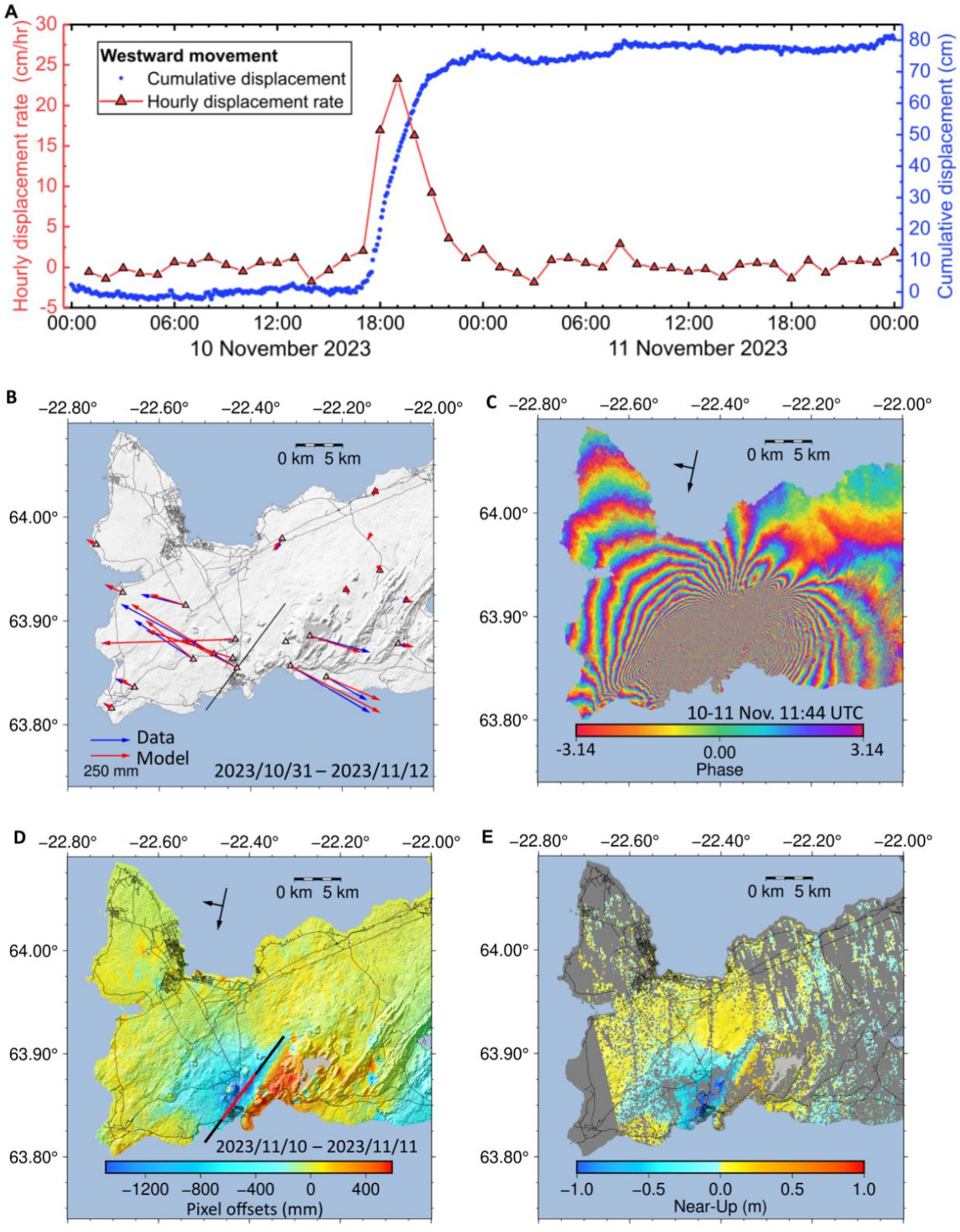
A
Westward movement
Cumulative displacement
Hourly displacement rate
Hourly displacement rate (cm/hr)
Cumulative displacement (cm)
10 November 2023
11 November 2023
B
Data
Model
250 mm
2023/10/31 – 2023/11/12
C
10-11 Nov. 11:44 UTC
-3.14
0.00
3.14
Phase
D
2023/11/10 – 2023/11/11
−1200 −800 −400 0 400
Pixel offsets (mm)
E
−1.0 −0.5 0.0 0.5 1.0
Near-Up (m)
0 km 5 km

Fig. 3

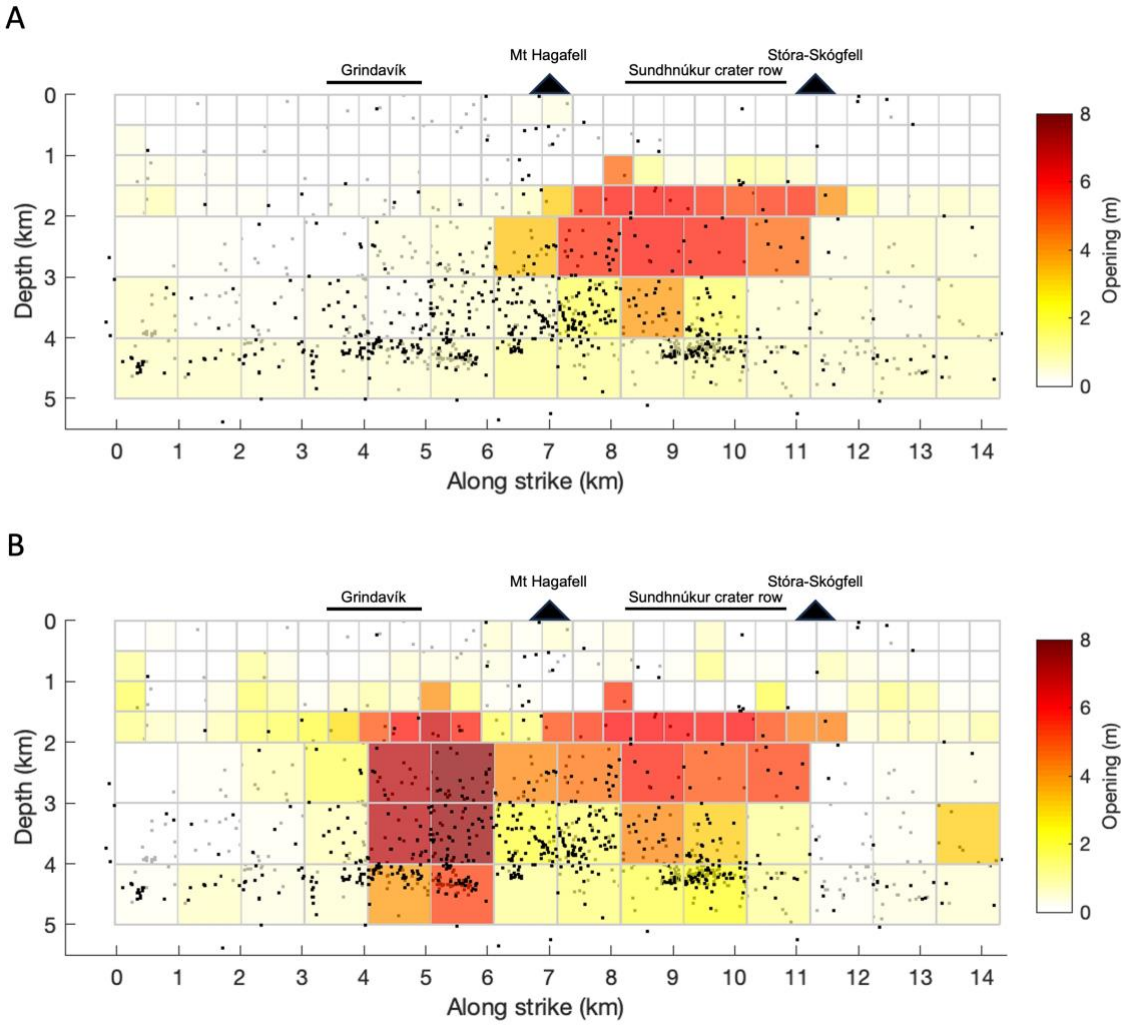
A
Grindavík
Mt Hagafell
Sundhnúkur crater row
Stóra-Skógfell
Depth (km)
Along strike (km)
Opening (m)
B
Grindavík
Mt Hagafell
Sundhnúkur crater row
Stóra-Skógfell
Depth (km)
Along strike (km)
Opening (m)

Fig. 4.

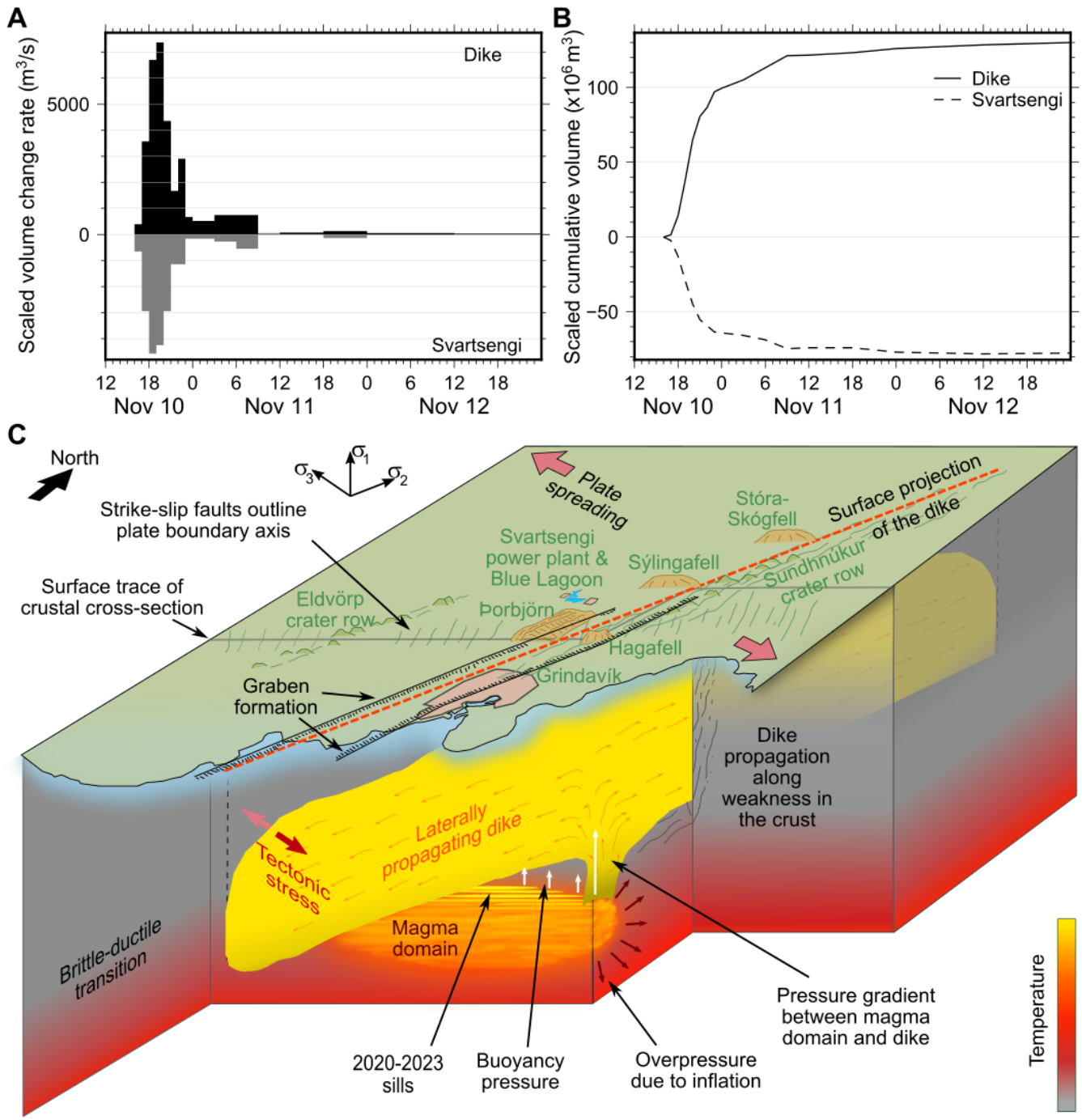
A
Scaled volume change rate (m³/s)
5000
0
Dike
Svartsengi
12 18 0 6 12 18 0 6 12 18
Nov 10 Nov 11 Nov 12
B
Scaled cumulative volume (x10⁶ m³)
100
50
0
−50
Dike
Svartsengi
12 18 0 6 12 18 0 6 12 18
Nov 10 Nov 11 Nov 12
C
North
σ1
σ2
σ3
Strike-slip faults outline plate boundary axis
Surface trace of crustal cross-section
Plate spreading
Stóra-Skógfell
Surface projection of the dike
Svartsengi power plant & Blue Lagoon
Sýlingafell
Sundhnúkur crater row
Eldvörp crater row
Þorbjörn
Hagafell
Grindavík
Graben formation
Dike propagation along weakness in the crust
Laterally propagating dike
Tectonic stress
Magma domain
Brittle-ductile transition
2020-2023 sills
Buoyancy pressure
Overpressure due to inflation
Pressure gradient between magma domain and dike
Temperature

Fig. 5

Supplementary Materials for

Fracturing and tectonic stress drives ultra-rapid magma flow into dikes

Authors: Freysteinn Sigmundsson[1]*, Michelle Parks[2], Halldór Geirsson[1], Andrew Hooper[3], Vincent Drouin[2], Kristín S. Vogfjörd[2], Benedikt G. Ófeigsson[2], Sonja H. M. Greiner[1,4,5], Yilin Yang[1], Chiara Lanzi[1], Gregory P. De Pascale[1], Kristín Jónsdóttir[1], Sigrún Hreinsdóttir[6], Valentyn Tolpekin[7], Hildur María Friðriksdóttir[2], Páll Einarsson[1], Sara Barsotti[2]

Affiliations:
[1] Nordic Volcanological Center, Institute and Faculty of Earth Sciences, University of Iceland, Reykjavik, Iceland
[2] Icelandic Meteorological Office, Reykjavik, Iceland
[3] COMET, School of Earth and Environment, University of Leeds, Leeds, UK
[4] Department of Earth Sciences, Uppsala University, Uppsala, Sweden
[5] Center for Natural Hazard and Disaster Science (CNDS), Uppsala/Stockholm/Karlstad, Sweden
[6] GNS Science, Lower Hutt, New Zealand
[7] ICEYE OY, Maarintie 6, 02150 Espoo, Finland

Correspondence to: fs@hi.is

This PDF file includes:

Materials and Methods

GNSS data and analysis

GNSS data used in this study are from continuously running stations on the Reykjanes Peninsula, with the addition of one campaign station (SVAR) to display long-term deformation in the area (fig. S1). The stations are operated as a collaboration of the Icelandic Meteorological Office; Institute of Earth Sciences, University of Iceland; and HS-Orka. During the October 27 - November 10 inflation phase, nine new stations were fully installed, and nine more became operational on or following November 11 (not used in this study; fig. S1). In general, processing longer batches of GNSS data results in better accuracy. The GNSS data are processed in several ways to achieve balance in appropriate time resolution and accuracy, all using ultra-rapid (predicted) and rapid IGS orbits and FES2004 ocean loading corrections (*59*):

(a) 5-min solutions: Kinematic solutions output at a 5-minute interval are calculated using precise-point-positioning (PPP) in the GIPSY/OASIS II software (*60*). Stochastic filtering properties in the software were set to "-kin_sta_xyz 1.0e-1 6.0e-7 300 RANDOMWALK". These filtering values allow for rapid changes in position, without resulting in excessive noise in the solutions. The resulting time series are in the ITRF2014.

(b) 8-hr solutions: Near real time 8-hour GNSS site positions were estimated using GAMIT/GLOBK 10.7 software (*61*), using 24-hour running reference station data to constrain site position in ITRF14/IGB14. The processing approach is described in Parks et al. (*13*)

(c) 24 hr-solutions: We run three different processing schemes for 24-hour solutions: (i) Daily PPP single-station solutions using GIPSY/OASIS II with single-site ambiguity resolution (*62*). (ii) Daily site positions estimated using GAMIT/GLOBK and solving for satellite orbit parameters during the analysis. (iii) A separate run of daily solutions using GAMIT/GLOBK, using fixing satellite orbit parameters to published ones and yielding results in ITRF08. Furthermore, GNSS data are streamed in real-time for baseline processing using RTKLIB (*63*), however those results are not used in this study.

InSAR analysis

SAR images from ICEYE, COSMO-SkyMed, Sentinel-1, and TerraSAR-X satellites constellations have been acquired to cover the October-November unrest in the Svartsengi area (fig. S10). Best image pairs were used to form interferogram using ISCE2, the Interferometric synthetic aperture radar Scientific Computing Environment (*64*). The phase unwrapping was done using SNAPHU (*65*). Topography was corrected using a 10-m DEM from Landmælingar Íslands (the National Land Survey of Iceland). No atmospheric correction was applied. Pixel offset tracking was also conducted on the pairs covering the November 10 – 11 dike as they allow to measure deformation where interferometry loses signal because of aliasing (fig. S11). It was done using ISCE2 for the COSMO-SkyMed and Sentinel-1 images and using internal tool from ICEYE for their own images. Only the range pixel offsets were used in this study.

Seismic data and analysis

Seismicity is monitored by the Icelandic Meteorological Office (IMO), where earthquakes are recorded on the SIL national seismic network and automatically located by the SIL analysis system (*66, 67*). The events are then manually reviewed, revised and updated as required, using a one-dimensional velocity model (SIL model). During the 18 days covered in this paper, around thirty thousand earthquakes were located on the Reykjanes peninsula (RP) by the automatic SIL system. At the time of writing only roughly 10% of the events have been reviewed and many of the larger events have not been fully reviewed. In the paper, reviewed events are used to present the earthquake distribution and its variation in time, but a selected

set of reviewed events is used to map the extent, strike and dip of the dike through the use of high-precision earthquake relocations (*68*). This method has been successfully used in previous mapping of dyke intrusions in Icelandic volcanoes (*1*, *69*). Event magnitudes, M (local moment magnitude) are calculated in the SIL software (*70*). These can be somewhat underestimated for the larger events. Moment magnitudes, M_W are shown for a few events, based on attenuation relations for Peak Ground Velocity (PGV) in Iceland (*71*). M_W for two of the larger events displayed in figures are obtained from the GFZ GEOFON Moment Tensor solution, available at: https://geofon.gfz-potsdam.de/old/eqinfo/list.php?mode=mt. These are marked with an asterisk in Fig. 1D and S13.

To improve seismic monitoring of the ongoing unrest on RP, additional waveform data from eight stations owned by the Czech Academy of Sciences (CAS) and operated by Iceland GeoSurvey (ÍSOR) are used in the routine locations. Three of these stations (lsf, iss and lag) are used in the relative relocations.

Supplementary Text

Geodetic modelling

We inverted the geodetic data using a Bayesian approach with a Markov-chain Monte Carlo method based on the Metropolis Hastings algorithm, using a modified version of GBIS software (*72*) to obtain a range of source parameters for each time interval that can explain the observed deformation.

For the inflation interval (Fig. 2) we used a descending COSMO-SkyMed interferogram spanning 17/10/2023 to 01/11/2023, an ascending COSMO-SkyMed interferogram from spanning 18/10/2023 to 02/11/2023 and GNSS data spanning 27/10/2023 to 03/11/2023. For the InSAR data, the variance-covariance was calculated assuming an exponential covariance function (*60*) with range of 4.5 km, sill value of 100 mm^2 and nugget value of 1 mm^2. For the GNSS data the variance was based on the formal errors and covariance assumed to be zero. We tried inverting for a point pressure source (*19*) and an opening rectangular dislocation (*18*) and found that the data were best fit by a sill-like opening rectangular source. We assumed a Poisson's ratio of 0.27 (also for subsequent models) and all of the source parameters were allowed to vary, with wide bounds defined a priori.

For the diking interval up until 12/11/2023 (Figs. 3 and 4) We used range offsets from three different satellites: ICEYE descending data acquired at 11:44 on 10/11/2023 and 11/11/2023 from track 26, COSMO-SkyMed ascending data acquired at 06:31 on 03/11/2023 and 11/11/2023 from track 33, and Sentinel-1 ascending data acquired at 19:00 on 31/10/2023 and 12/11/2023 from track 16. We also used GNSS data spanning 19:00 31/10/2023 to 19:00 12/11/2023. Large vertical values were ignored for stations GRIC and THOB as they were inconsistent with the range offsets and appeared to reflect local deformation related to graben faulting.The variance-covariance for the range offsets was based on an exponential covariance function with range 6 km and sill 400 mm^2, and variable nugget of Sentinel-1: 900 mm^2, COSMO-SkyMed: 10,000 mm^2 and ICEYE: 5000 mm^2. For the ICEYE data we set the sill value higher at 10,000 mm^2 to allow for significant deformation that occurred between the second acquisition and the second Sentinel-1 acquisition. For the GNSS data, the variance was based on the formal errors multiplied by a factor of 10 and the covariance was assumed to be zero. Initially we solved for opening and strike-slip motion on a single rectangular dislocation (*19*) to represent the dike, and a deflating point pressure source (*20*) for the subsidence. The dike aligned very closely to our relocated seismicity, so we then fixed the location based on the seismicity. Subsequently we divided the dike into 158 patches and solved for opening and strike-slip motion on each one, while allowing the pressure source to vary freely. In a second iteration, we set the lower

bound for patches that opened more than 2 m in the diking inversion for the interval until 10/11/2023, to be equal to the optimal model for that time interval. In other words, we did not allow patches to close significantly once opened.

For the diking interval up until 10/11/2023 (Fig. 4) we used a COSMO-SkyMed descending interferogram from track 44 spanning 02/11/2023 to 10/11/2023, acquired at 19:35, and GNSS data covering the same time interval. The variance-covariance for the interferogram was based on an exponential covariance function with range 6 km, sill 400 mm^2 and nugget 1 mm^2. For the GNSS data the variance was based on the formal errors and covariance was assumed to be zero. We used the same rectangular dislocations for the dike as in the inversion for the interval up until 12/11/2023 and solved for opening and strike-slip motion. We also fixed the deflating point pressure source location to the position found in the longer interval.

For GNSS temporal inversion we use hourly displacements generated from 5-minute solutions by differencing positions made at each whole hour (00:00, 01:00, etc). These were used to infer the location of the dike at that time. This was done with a simple inversion process. The model is constituted of (i) a Mogi point source (*20*) with location fixed to the most probable solution from the combined InSAR and GNSS inversion for the whole interval (X, Y, depth) to account for the magma domain deflation beneath Svartsengi, (ii) an Okada dislocation (*19*) fixed within the same plane as used in the combined InSAR and GNSS inversion but with free dimension and opening within that plane. This amounts to a total of 6 parameters: volume change of the Mogi source, distance along the plane, length, width, depth, and tensile opening of the Okada dislocation. The best fitting model parameters were found using a simple grid search approach (Chi-Square estimator). The results are scaled such that the total cumulative volume for both the deflation source and the dike are equal to the most probable values found from the combined InSAR and GNSS solution. As a result, we can follow the temporal evolution of the dike and the magma body (figs. S22–S25).

Physical model

Volume change of an ellipsoid in an elastic halfspace due to a pressure change within it depends on the relative length of its half-axis (aspect ratio), its orientation, and depth (see Fig. 12 in reference *35*). For our representative geometry of the magma domain, we take 1/μ as an estimate of the compressibility of the chamber rather than 3/(4μ) which would be the value for a spherical source in full elastic space (*34*, *35*). Then the relation between volume change of the magma domain and pressure change is:

$$\Delta V_{Magma\ domain} = \frac{\mathrm{V}\Delta P}{\mu} = \frac{4\pi}{3}\frac{abc\Delta P}{\mu}$$

For a certain pressure change, the material within the magma domain will change volume due to compressibility (*27*) by the following amount:

$$\Delta V_{Compressibility} = \frac{\mathrm{V}\Delta P}{k} = \frac{4\pi}{3}\frac{abc\Delta P}{k}$$

Here (1/*k*) is the magma compressibility. The amount of magma inflow/outflow will be the sum of the above volumes:

$$\Delta V_{magma\ flow} = (\frac{1}{\mu} + \frac{1}{k})\frac{4\pi}{3}abc\Delta P$$

The ratio of the volume of magma flow and volume change of the magma domain is then:

$$\frac{\Delta V_{magma\ flow}}{\Delta V_{Magma\ domain}} = 1 + \frac{\mu}{k}$$

Supplementary figures

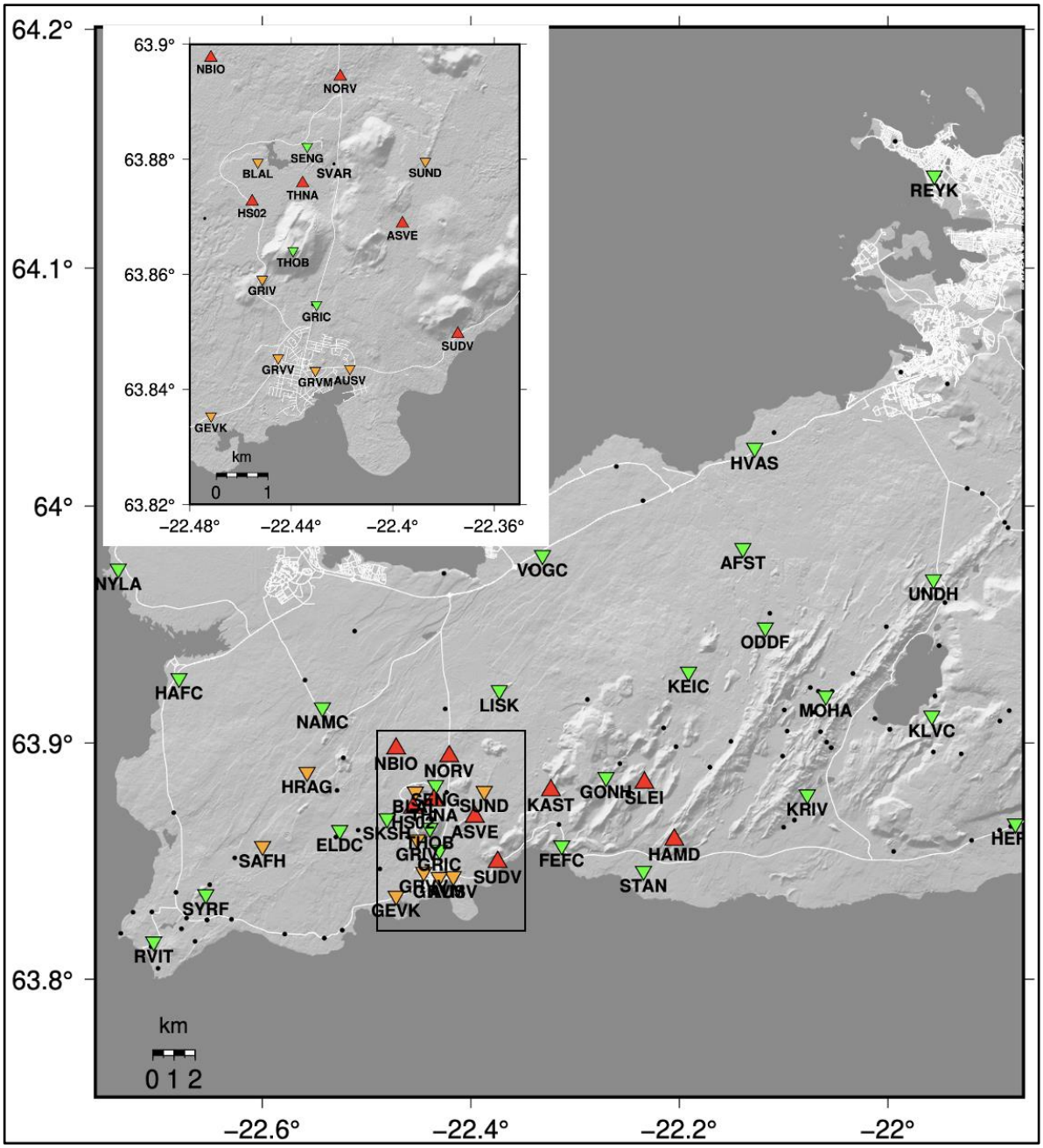

Fig. S1.
Map of all GNSS stations used in modelling. Inset shows a zoomed-in section around Grindavík and Svartsengi. Green triangles: pre-existing stations; red triangles: stations installed during the October 27 – November 10 2023 inflation phase; orange triangles: stations installed after the main dike formation on November 10. Black dots indicate GNSS campaign benchmarks.

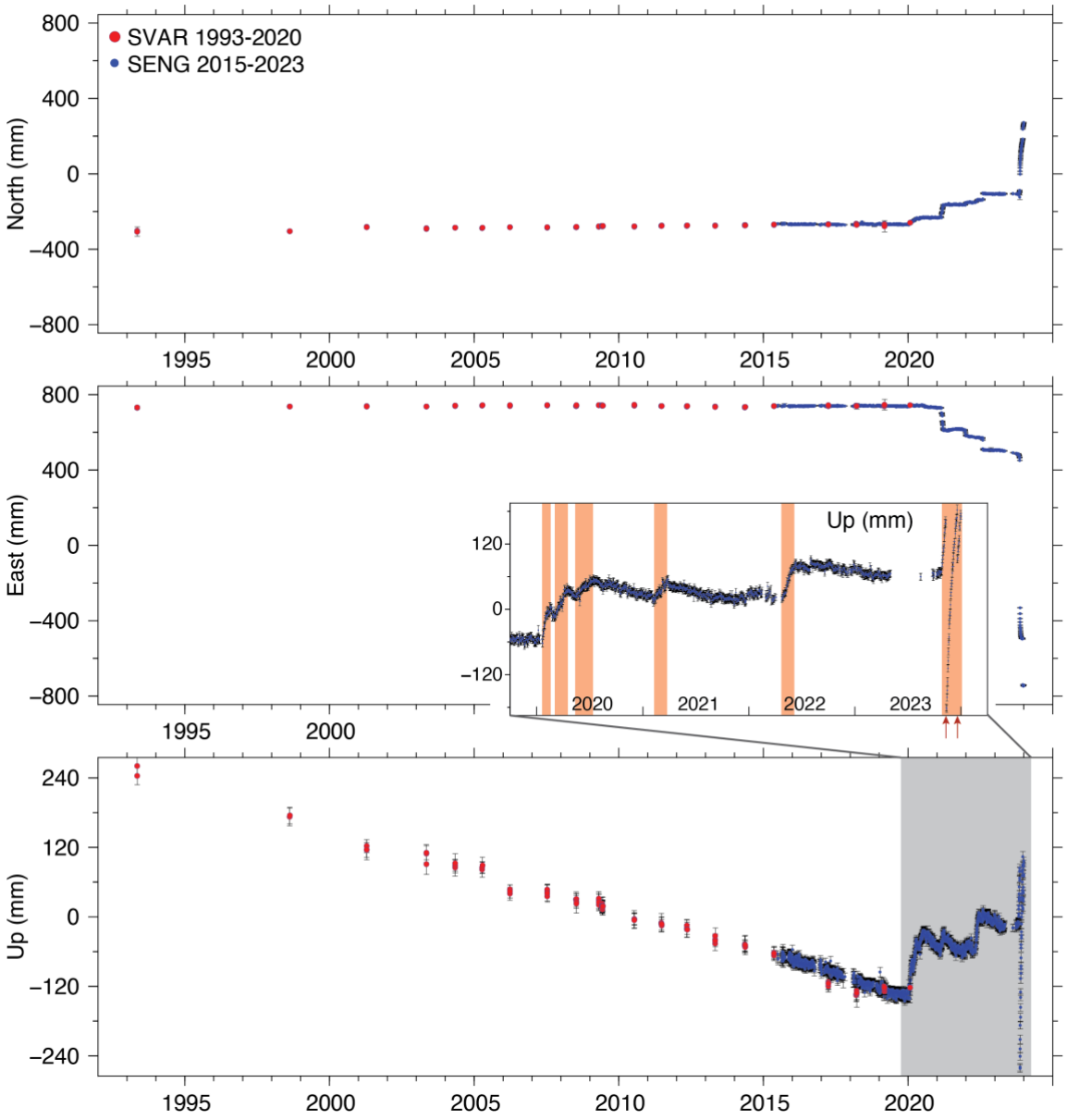

Fig. S2.
Long-term time series of deformation at Svartsengi. Continuous station SENG and near-by campaign site SVAR (locations in Fig. S1). GNSS data processing follows GNSS data and analysis section (*c*)-(ii) in Methods. Horizontal motion is de-trended relative to average motion in 2015 – 2020 and vertical motion is in the ITRF2014. Grey shaded region on bottom panel indicates period of unrest between 2020 – 2023, including inflation events and diking episodes in November and December 2023 (marked with red arrows).

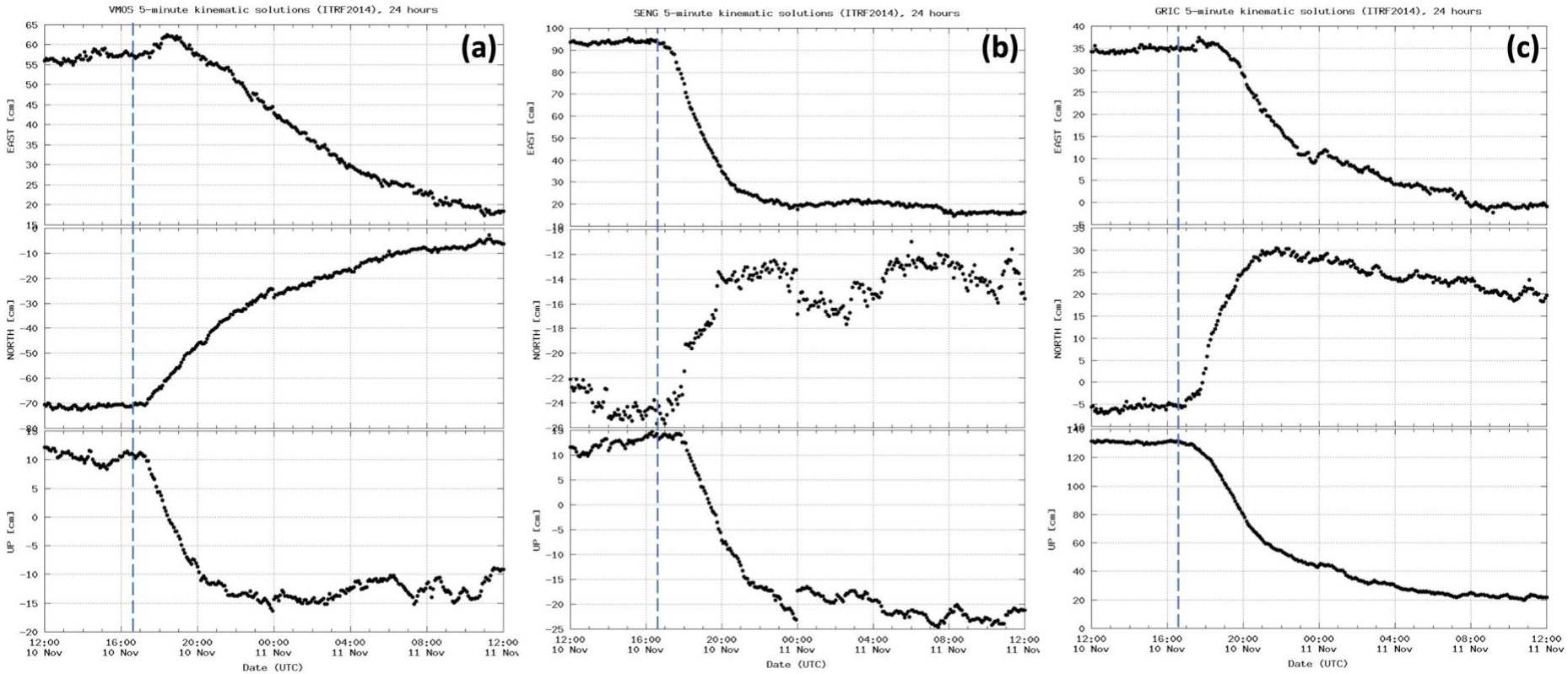

Fig. S3.
Examples of time series showing dike deformation. GNSS time series at stations VMOS (a), SENG (b), and GRIC (c) from 5-minute solutions. Vertical dashed line marks the earliest observed onset of deformation, at 16:40. As the dike started growing from the north, deformation is first observed in the northern part of the network (e.g. station SENG), then propagatig towards SSW. Station GRIC (c) is located on top of the dike, and shows a reversal in its north compenent as the dike propagates under it.

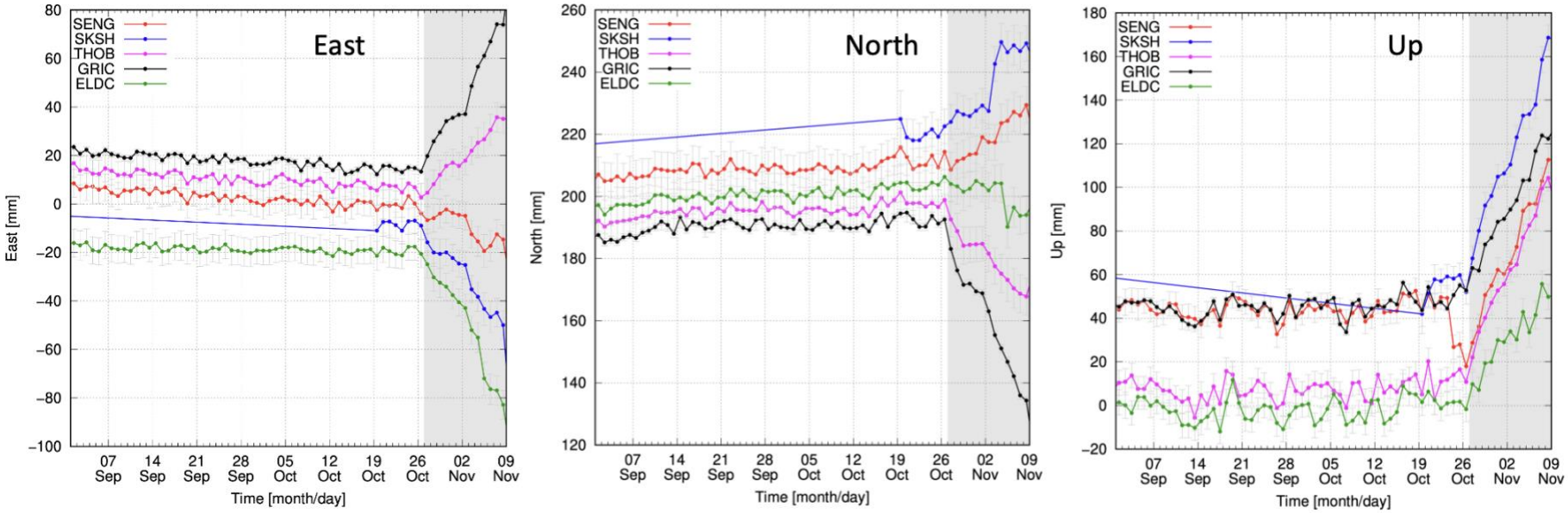

Fig. S4.
GNSS time series, 24-hr solutions, for the October 27 – November 10 inflation episode shown in East, north, and Up component of motion. The inflation period is marked by an abrubt change in deformation, high uplift rates (Up panel), and outward motion (East and North panels). See Fig. S5 for a mapview of horizontal motion during the inflation episode. GNSS data processing follows GNSS data and analysis section (c)-(i) in Methods.

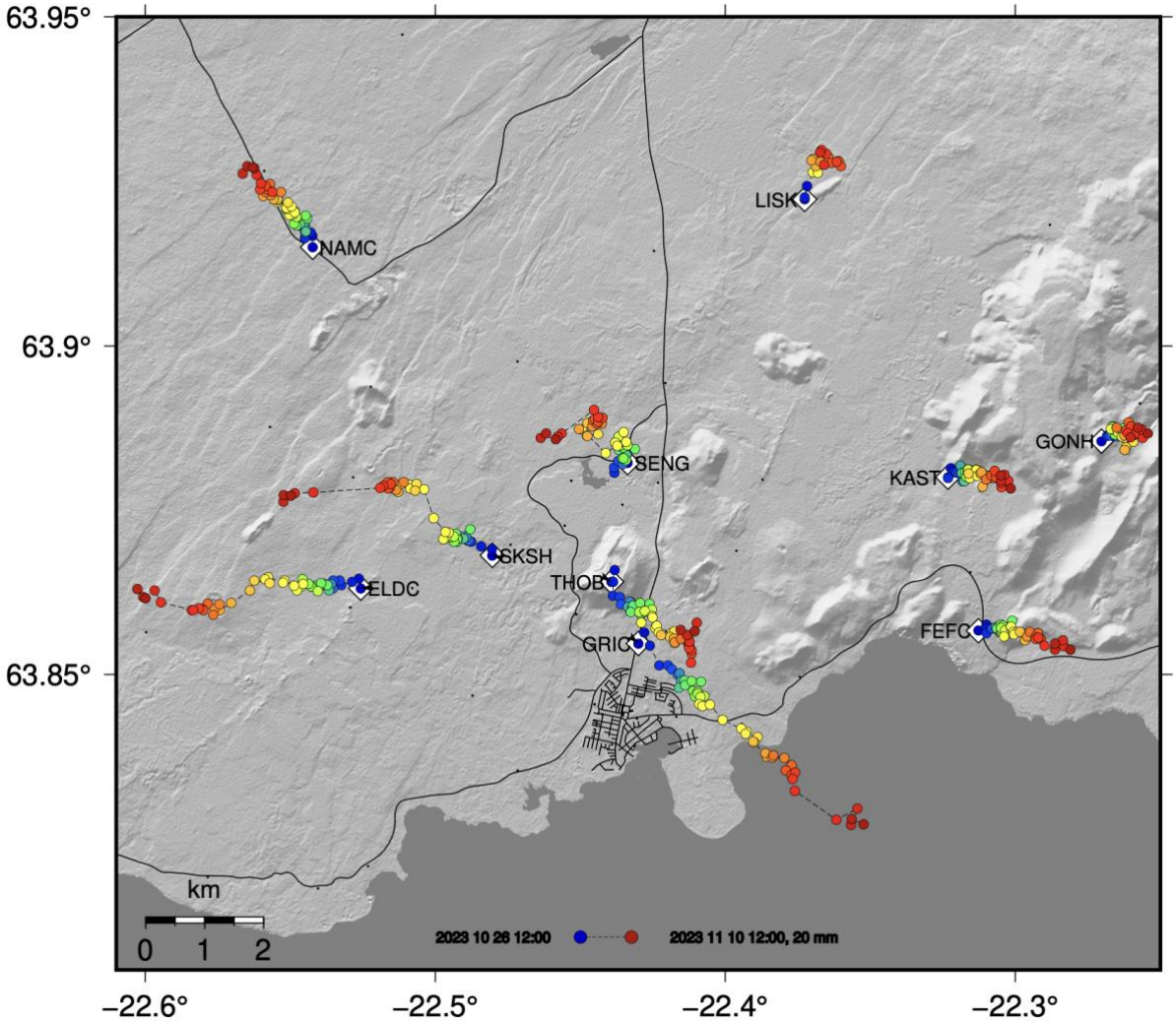

Fig. S5.
Horizontal displacements of GNSS stations, October 26 to November 10, 2023. 8-hour solutions using the GAMIT/GLOBK software are shown (see Methods). Scale is indicated at the bottom of the map. The station motions are color-coded according to time.

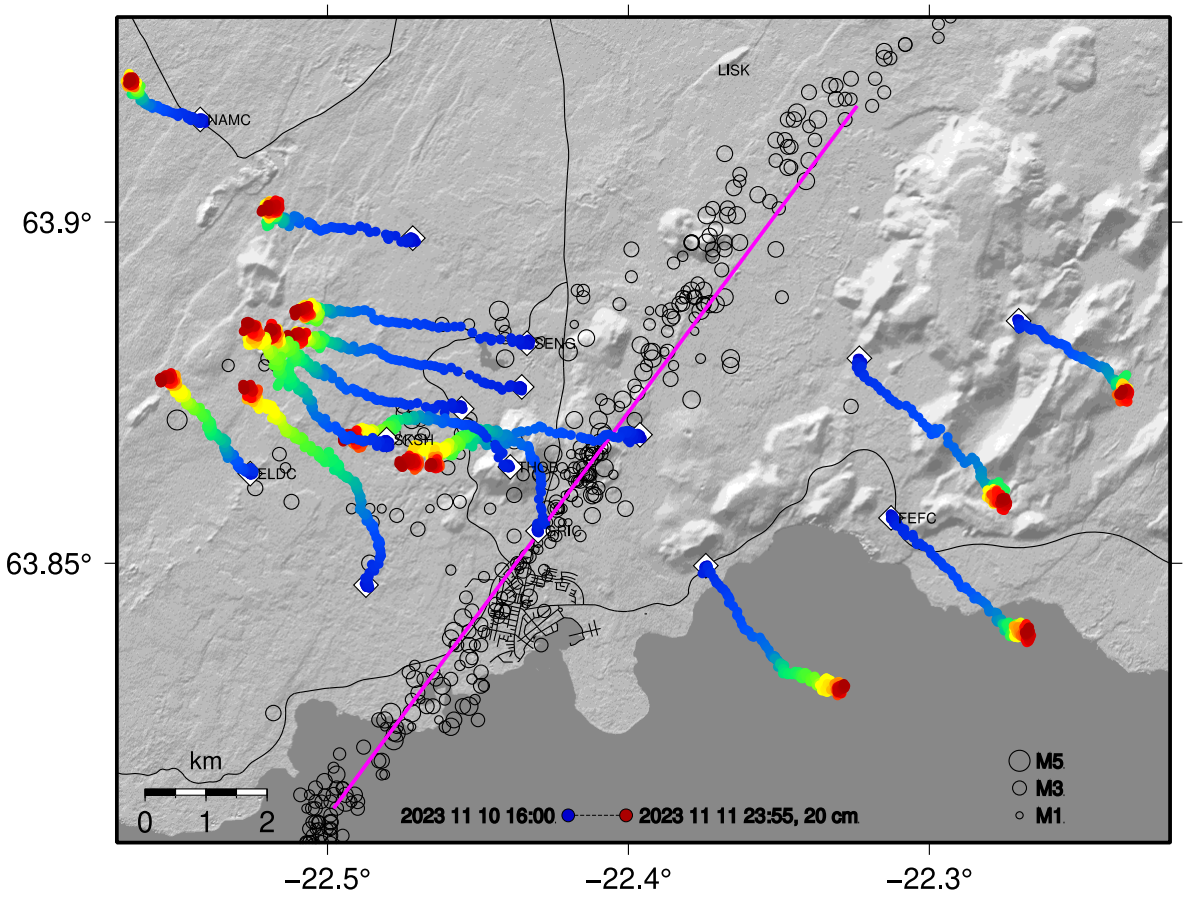

Fig S6.
GNSS observed dike ground deformation. Horizontal displacements of GNSS stations from 16:40 UTC on November 10, to 23:55 on November 11, 2023, from 5-minute solutions using the GIPSY/OASIS II software (see Methods). Scale is indicated at the bottom of the map. The station motions are color-coded according to time. Black circles show epicentres of manually located earthquakes in the same period, and magenta line indicates the trace of the dike according to the geodetic models.

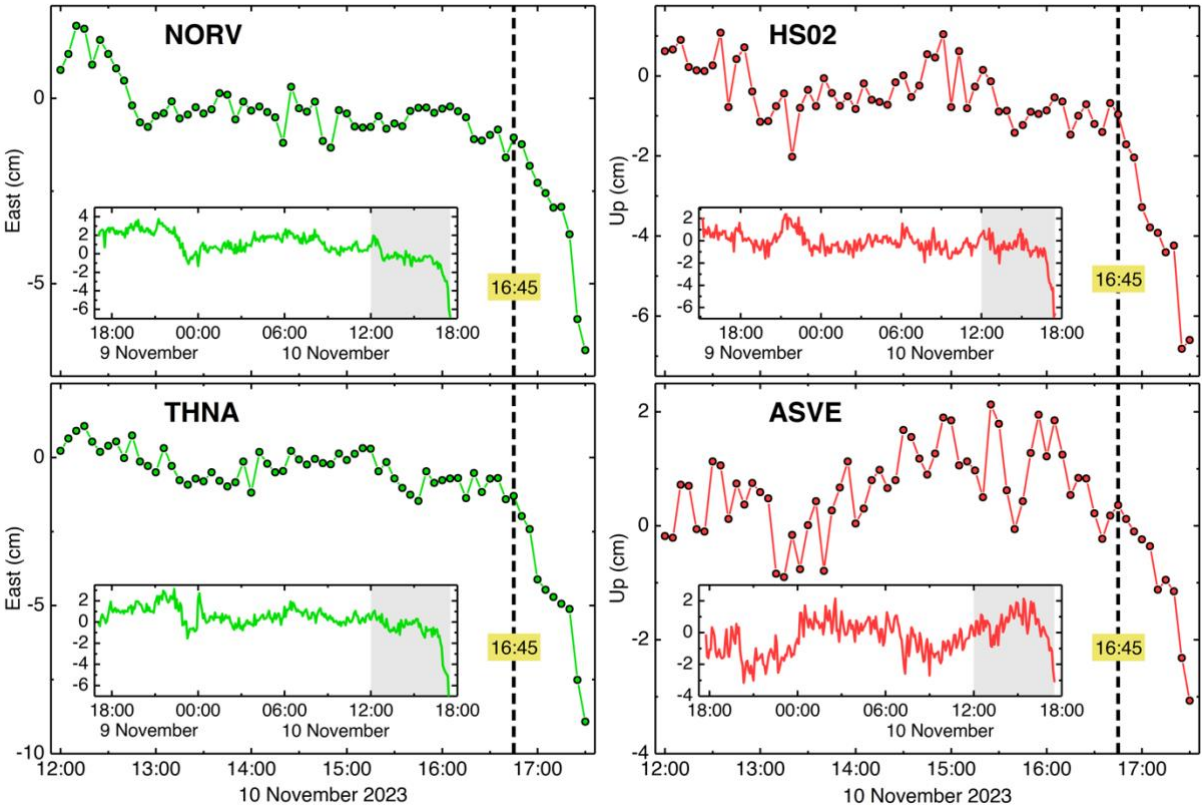

Fig. S7.
Onset of dike widening inferred from GNSS. Time series from 5-minute solutions (see Methods). Stations and coordinate components that have the clearest onsets are displayed. The inset for each panel shows a 24-hour timespan until 18:00 on November 10. Vertical dashed line indicates start time of deformation, 16:45 on November 10.

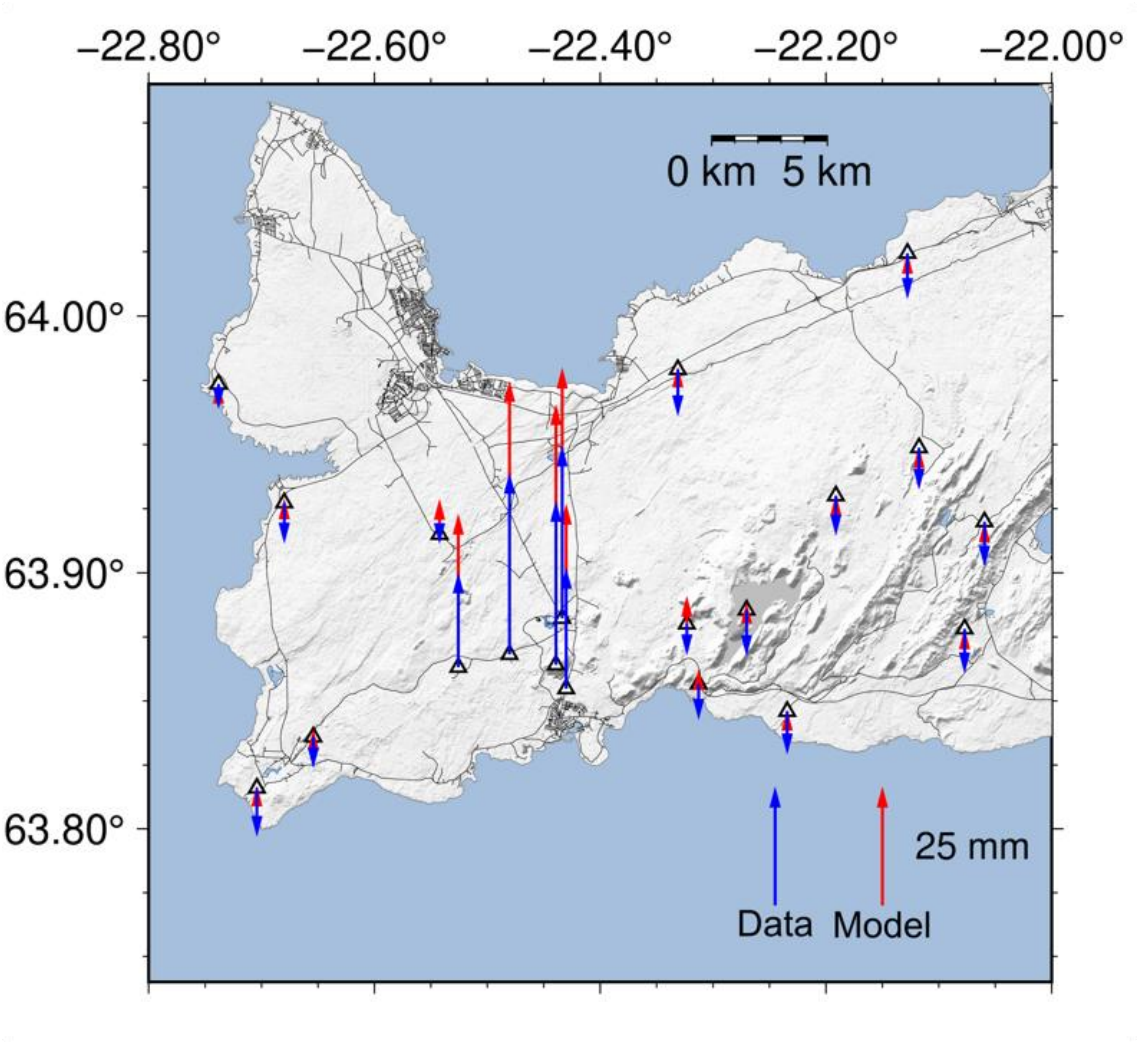

Fig. S8.
Inflation of Svartsengi, October 27 – November 10, 2023, with GNSS vertical displacements, observed and modelled.

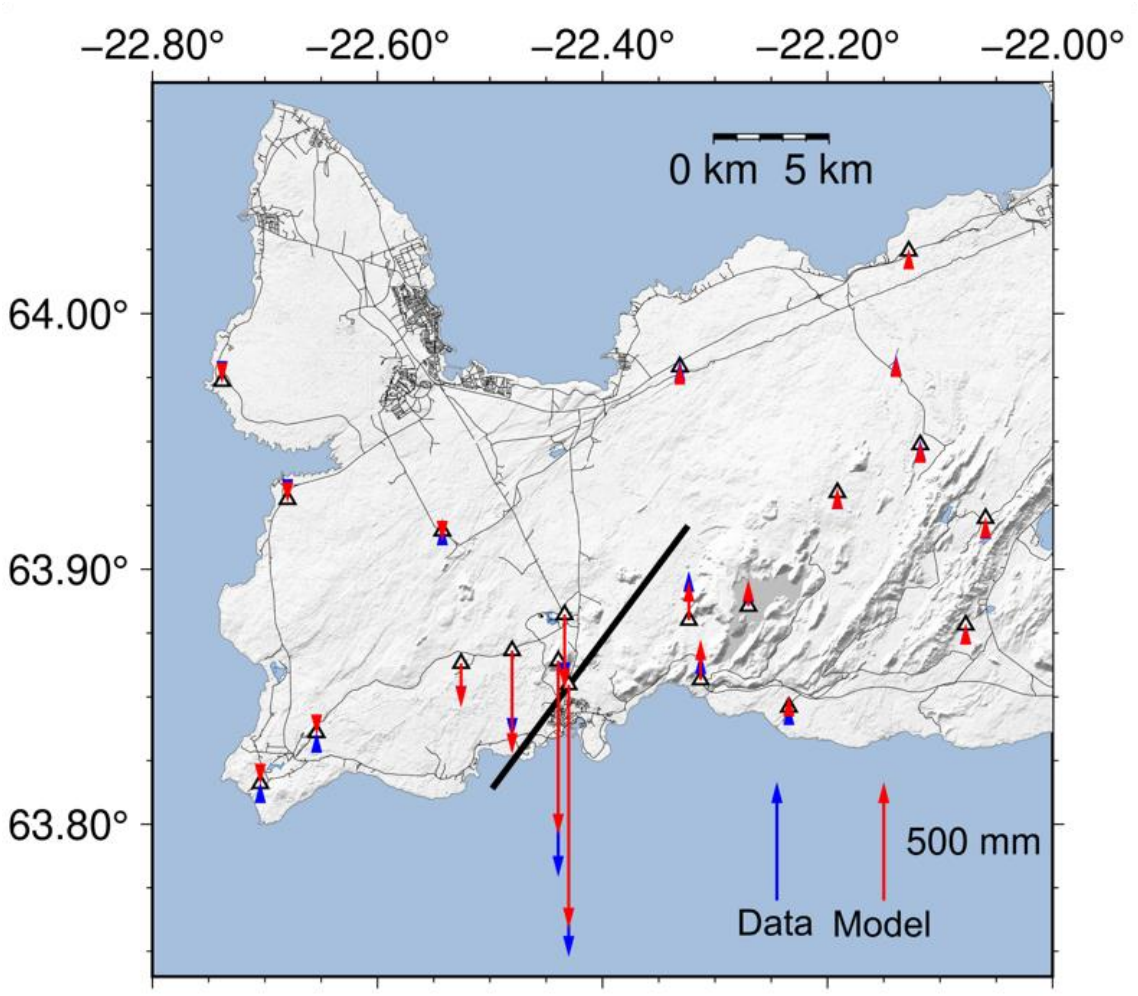

Fig. S9.
The dike formation on November 10 – 12, 2023, with GNSS vertical displacements, observed and modelled.

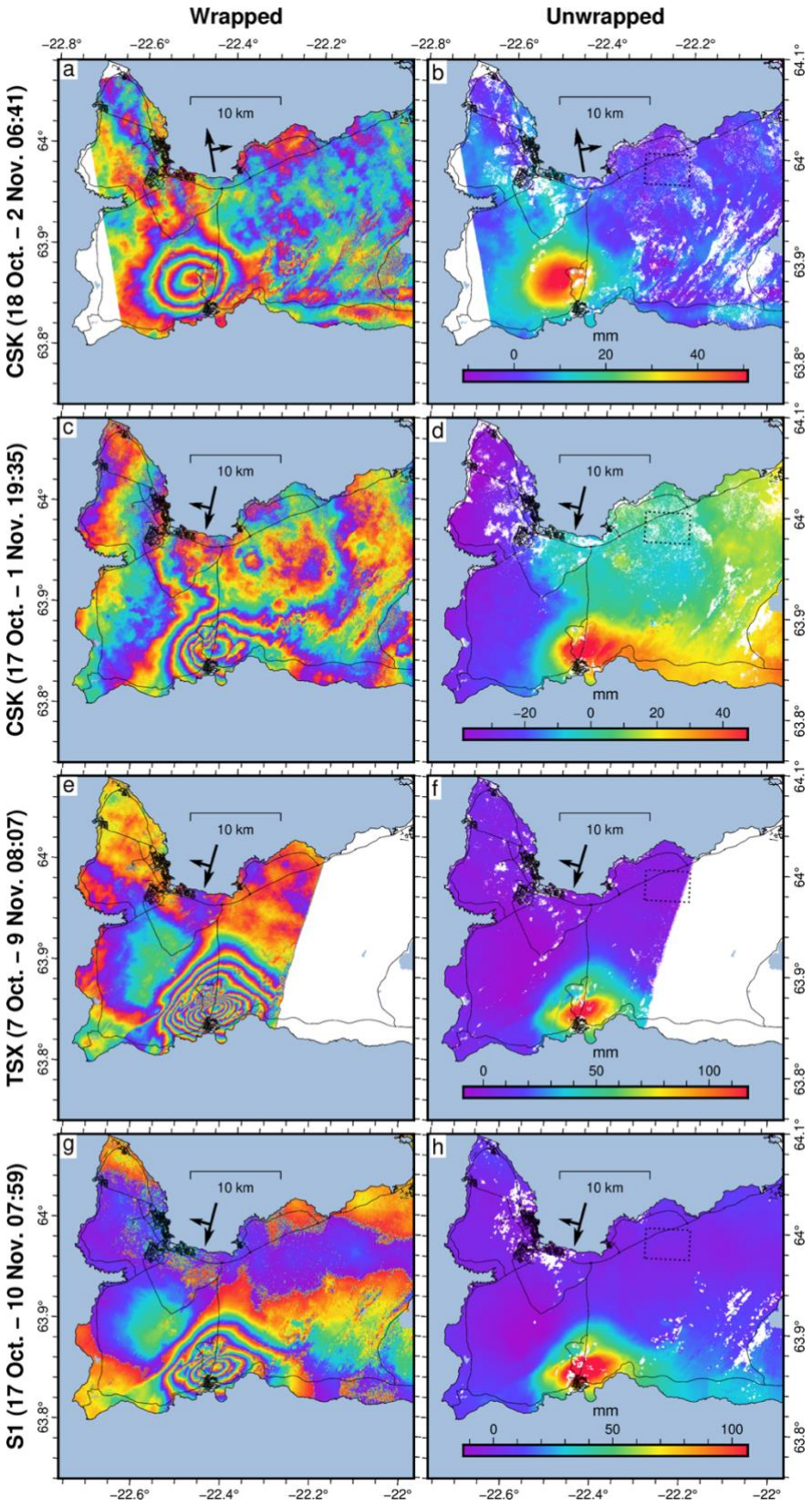

Fig. S10.
Interferogram series showing the inflation of Svartsengi in October and November 2023. Left panels (a, c, e and g) show the wrapped interferograms and right panels (b, d, f, and h) show unwrapped interferograms. Satellite and time span of interferograms shown on the right.

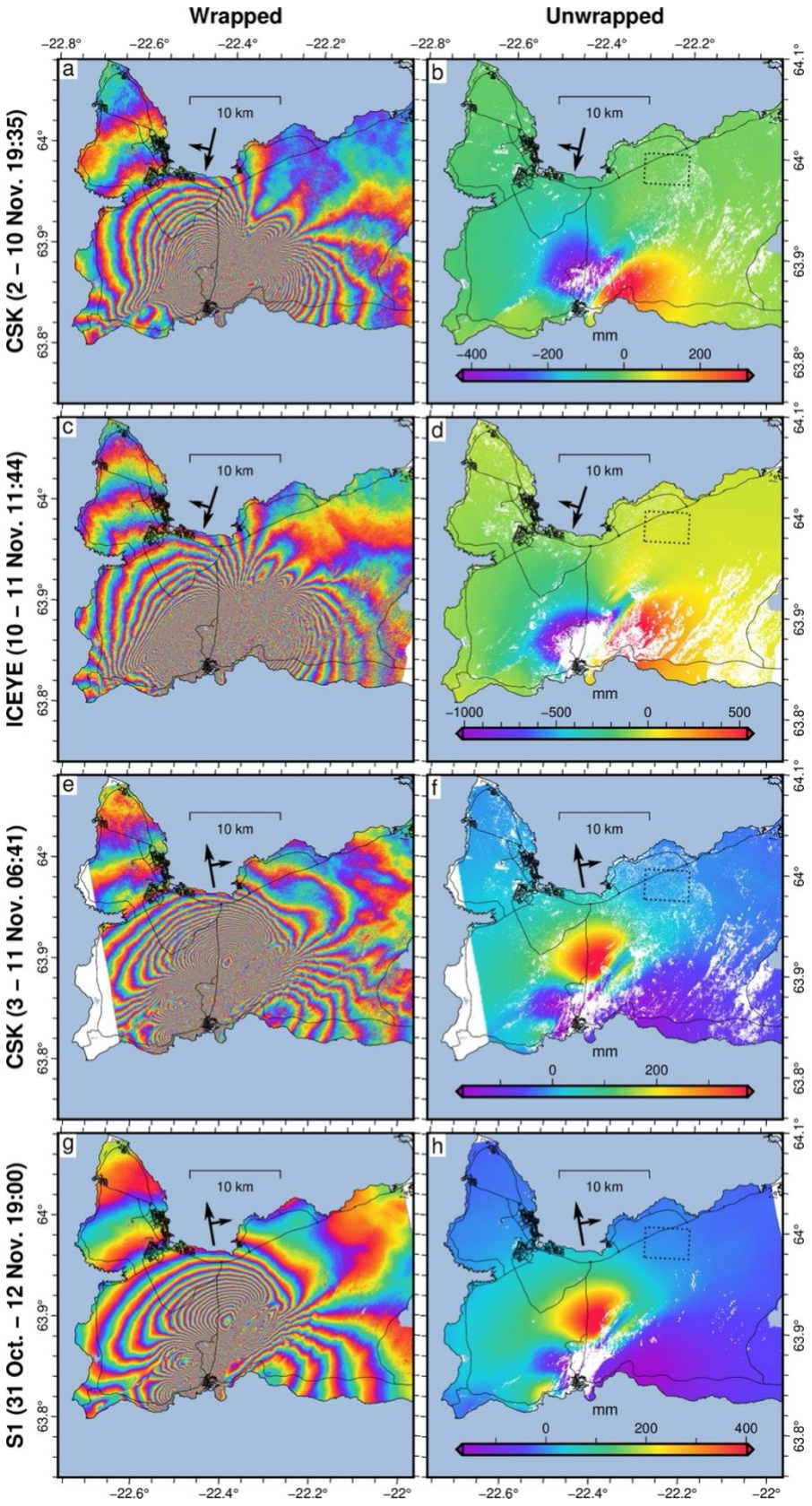

Fig. S11.
Interferogram series covering the dike formation period. Left panels (a, c, e and g) show the wrapped interferograms and right panels (b, d, f, and h) show unwrapped interferograms. Satellite and time span of interferograms shown on the right.

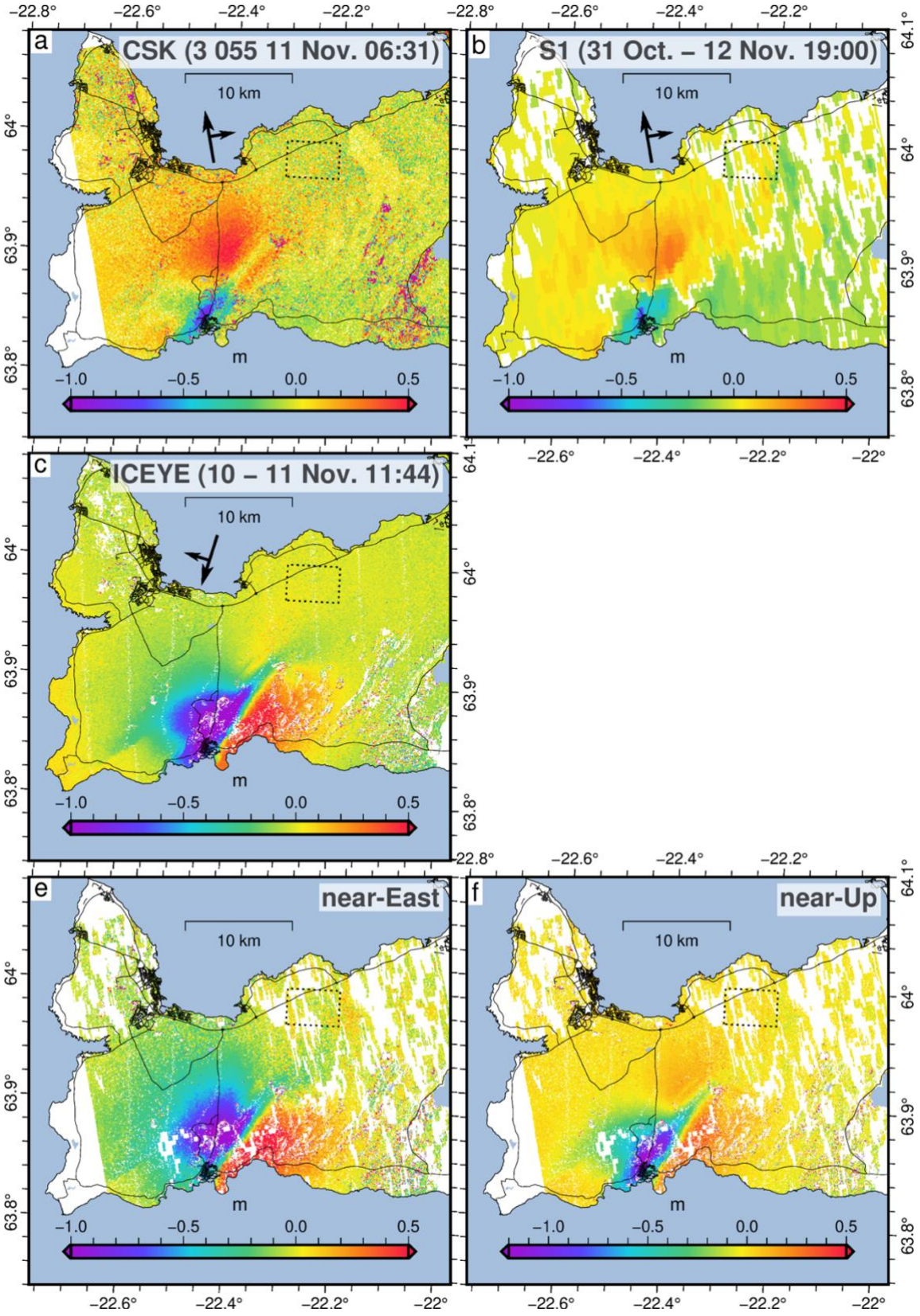

Fig. S12.
Range pixel offsets retrieved from different SAR satellite images covering the dike formation period (a-c), and their decomposition into approximate east displacement (near-East, panel e) and approximate vertical displacement (near-Up, panel f) (see ref. *22*).

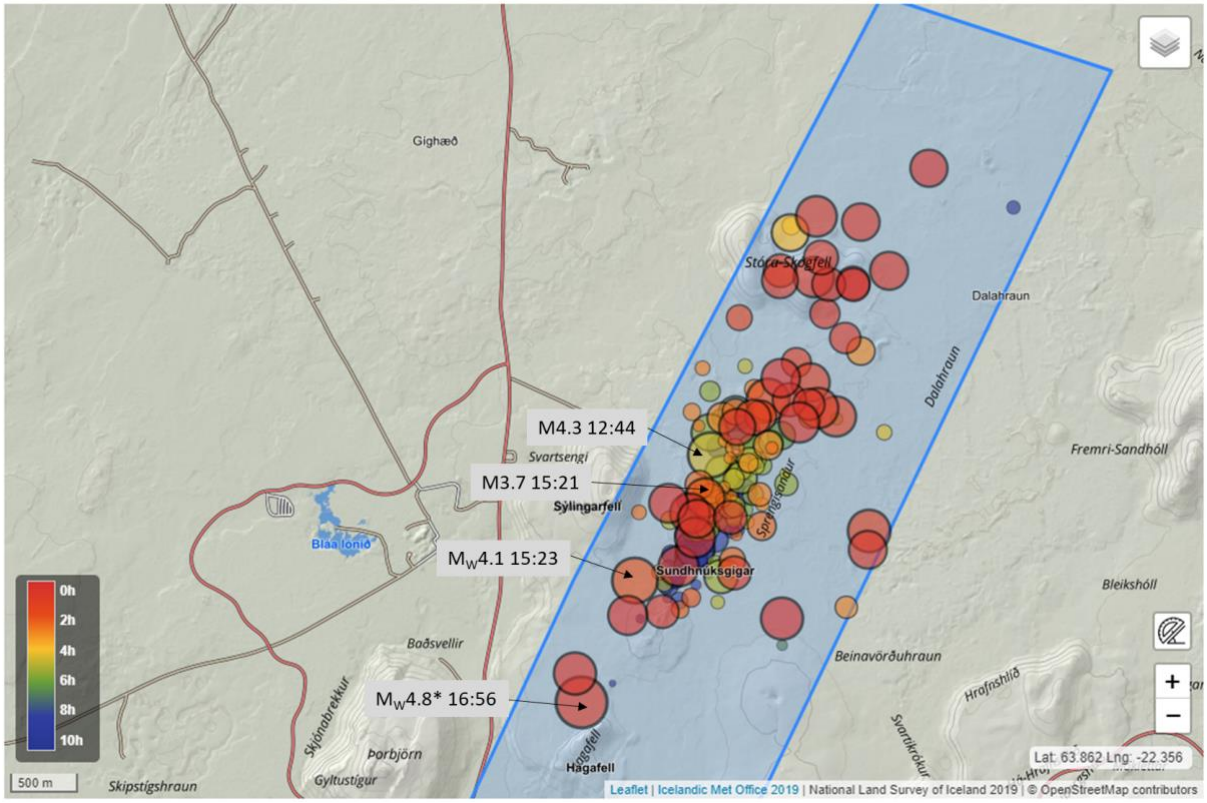

Fig. S13.
Chronology of seismicity during the initial phase of the dike formation, when propagation was mainly towards northeast. Reviewed events between 07:00 and 17:40 UTC on November 10, 2023 on the northern part of the dike. Events are color-coded according to time counting from 17:40. Time scale is shown on the lower left. Shortly after 7:00 of November 10 microseismicity beneath the Sundhnúkur crater row quickly picked up, starting at the southern end of the crater row (blue events in the figure), and gradually moving 3.5 km northward to Stóra-Skógfell over the next 8.5 hours, with an average speed of 0.1 m/s. The largest event occurring at the crater row during this time was a M_W4.3 at 12:44. Following two significant earthquakes, a M3.7 at 15:21 and a M_W4.1 at 15:23, beneath the crater row's southern end, the seismicity continued to move north-eastward, with a double pace (0.2 m/s) and much higher intensity, reaching its northern margin at 22:00, 8.5 km from where it initially started. Earthquake source depths remained steady at around 5-km depth below the surface during the slower advance, but during the faster pace, more events than before were generated at shallower depths. Only a few of the ~25 $M_W \geq 4$ earthquakes occurred on the northern segment during the propagation of seismicity. At the end of this period a M_W4.8* earthquake occurred at the northern end of Mt. Hagafell.

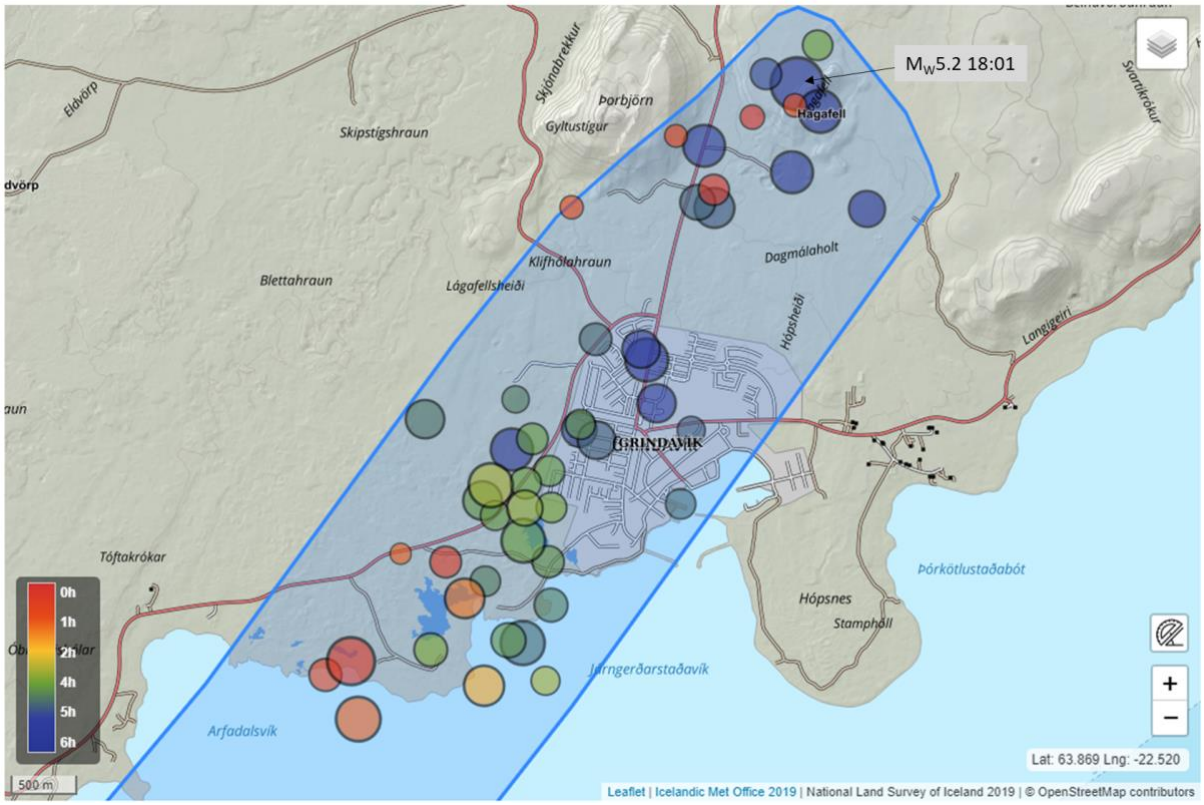

Fig. S14.
Chronology of seismicity in the second phase of the dike formation, when propagation was extremely fast and mainly towards south. Reviewed events from 18:00 to midnight on 10 November are displayed, encompassing the time period of the Mw5.2 event at 18:01 at Mt. Hagafell. The seismic moment of the event is a function of the crustal shear modulus (μ), the slip, and the area of the fault. Assuming same μ and a slip of ~70 cm gives an estimate of fault dimension of ~3-4 km, indicating that the event ruptured a several-km-long fault plane. Its mechanism was dominated by normal faulting (as determined by the SIL analysis software), striking in the general direction of the dike. The event distribution following the event shows very fast propagation of seismicity, with earthquakes having already occurred under Grindavík at 18:30 – 18:45, and by 19:30 – 19:45, earthquakes were starting to be detected south of the town, suggesting the locations were indeed also showing that the dike intrusion was already under Grindavík. The seismicity continued to advance out to a distance of ~10 km from the start near Sundhnúkur. The initial southward propagation velocity from Hagafell in the first 1.5 hours was 0.9 m/s but slowed down to about 0.5 m/s at the southern end which was reached before midnight. Earthquake depths were mostly around 5-km depth.

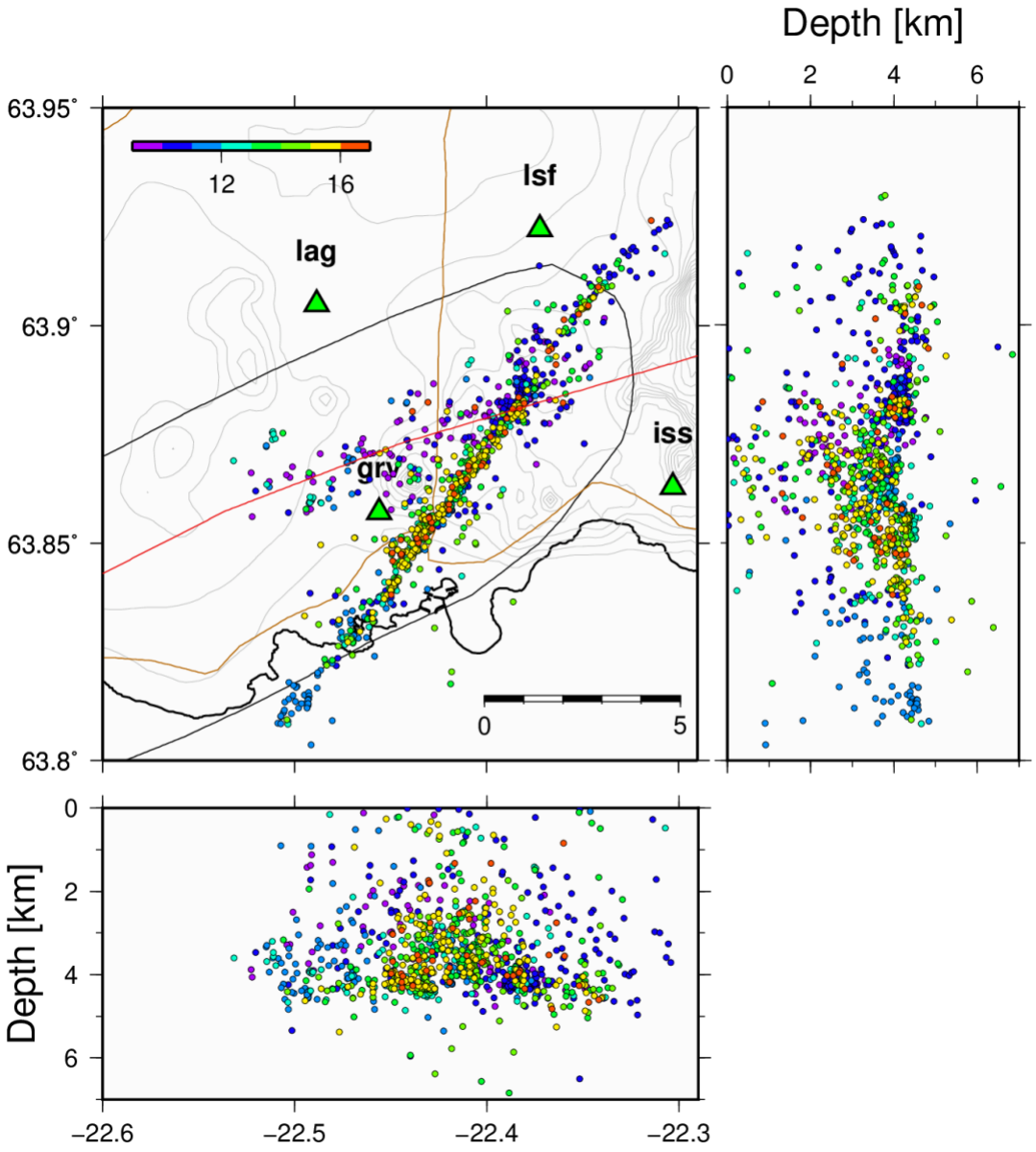

Fig. S15.
Relocated earthquakes defining the dike. The upper-left map shows eleven hundred microearthquakes recorded between November 9 and 16, 2023, color-coded according to time of occurrence. Time scale is shown at the top. Events occurring on November 10 are dark blue. The events are relatively relocated using cross-correlation of waveforms from 20 seismic stations in SW Iceland (*59*). The event distribution defines an over-all strike of the dike N35°E and dip of 90°. RMS deviation of the 875 events defining the best fitting plane is 170 m. The northernmost and southernmost parts of the dike have a slightly more easterly strike. Maximum depth of the events is ~4.5 km, shallowing in the central area to 4 km depth. The shallower overall depth of the relocated events, is mostly due to the use of a velocity model more appropriate for Reykjanes peninsula, which is slightly different from the standard SIL velocity model used in the manual locations of all events in Iceland. The plate boundary (shown with a red line) crosses the dike near the Sundhnúkur crater. The four closest stations are indicated by green triangles, three of them (lag, lsf and iss) are owned by the Institute of Geophysics, Czech Academy of Sciences, and operated by the Iceland GeoSurvey. The upper-right map shows the cross section viewed from East. The lower map shows the cross section viewed from south.

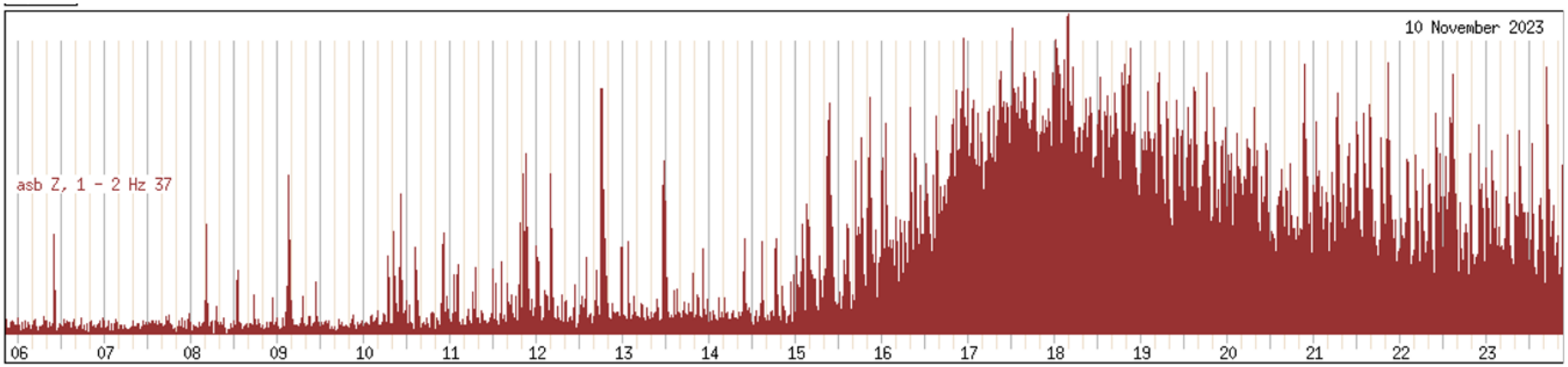

Fig. S16.
Real-time seismic amplitude (RSAM). Normalized vertical component RSAM during 6:00 – 24:00 on November 10 from the seismic station asb (Ásbjarnarstaðir/BORG) at 110 km distance in western Iceland. The time series, which represents 1-minute-averages of the band-pass filtered vertical component seismogram, shows the onset of the seismic swarm around 7:00, the growing intensity of the seismicity and magnitudes. The peak at 15:23 represents the Mw4.1 event which started the southward migration of seismicity, the one at ~18:00 represents the Mw5.2 at Hagafell, which allowed the propagation speed of the dike to escalate. The continuous swarm from around 16:00 to midnight contains round 20 Mw>4 and many more of Mw>3. The largest amplitude at 18:09 represents a triggered M5.3 earthquake at Eldvörp.

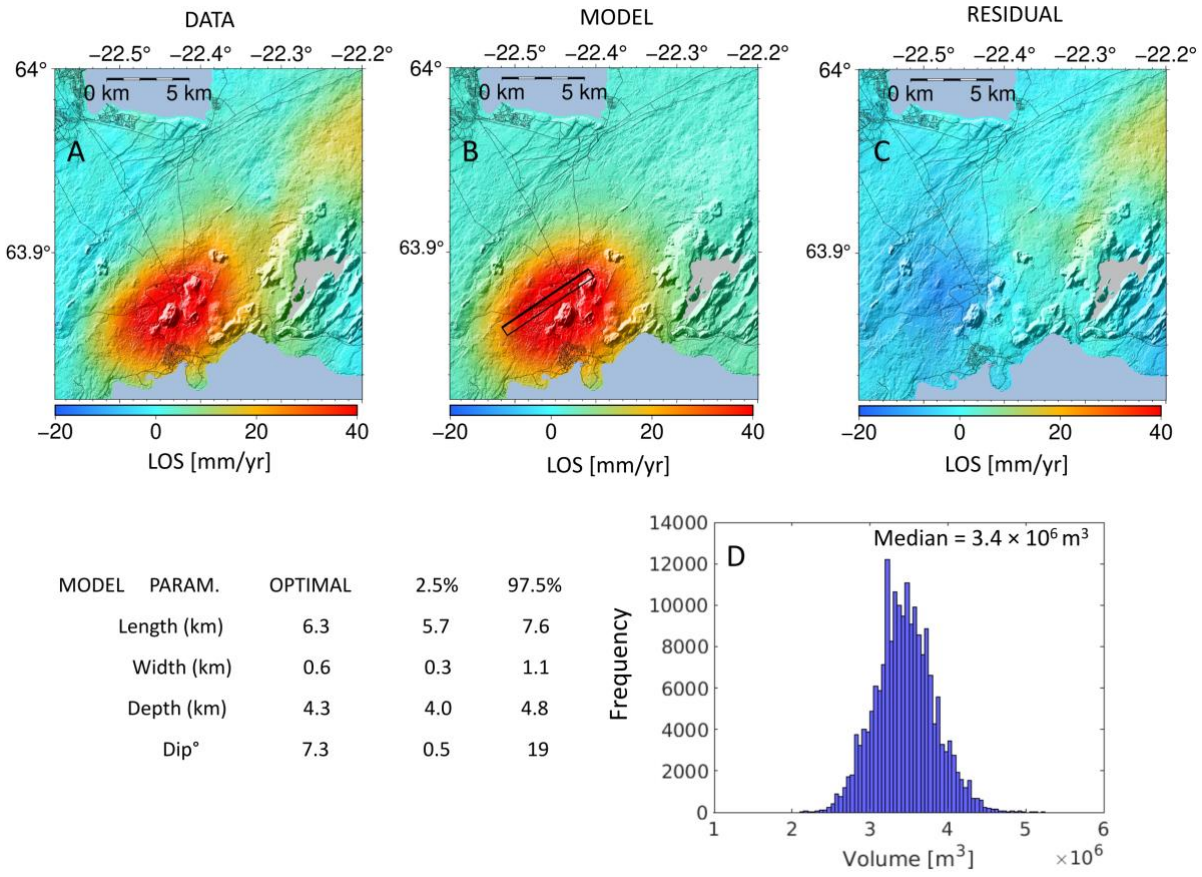

Fig. S17.
Uplift period at Svartsengi April 15 – June 21, 2022. Predicted displacements for a best fitting sill model and observations are compared. The thicker black line indicates the inferred surface projection of the sill at surface, while the thinner indicates the projection of the bottom part of the sill. (A) InSAR LOS data (time period: 2022-04-15 to 2022-06-21), (B) best-fit model prediction and (C) residual for the T110 TerraSAR-X image. (D) Estimated volume of the sill. The inverted model parameters are displayed on the bottom-left of the figure, where the columns show the optimal fit, and the 2.5 and 97.5 percentiles of posterior probability density functions. The range spanned by the 2.5 and 97.5 percentiles is the 95% confidence interval.

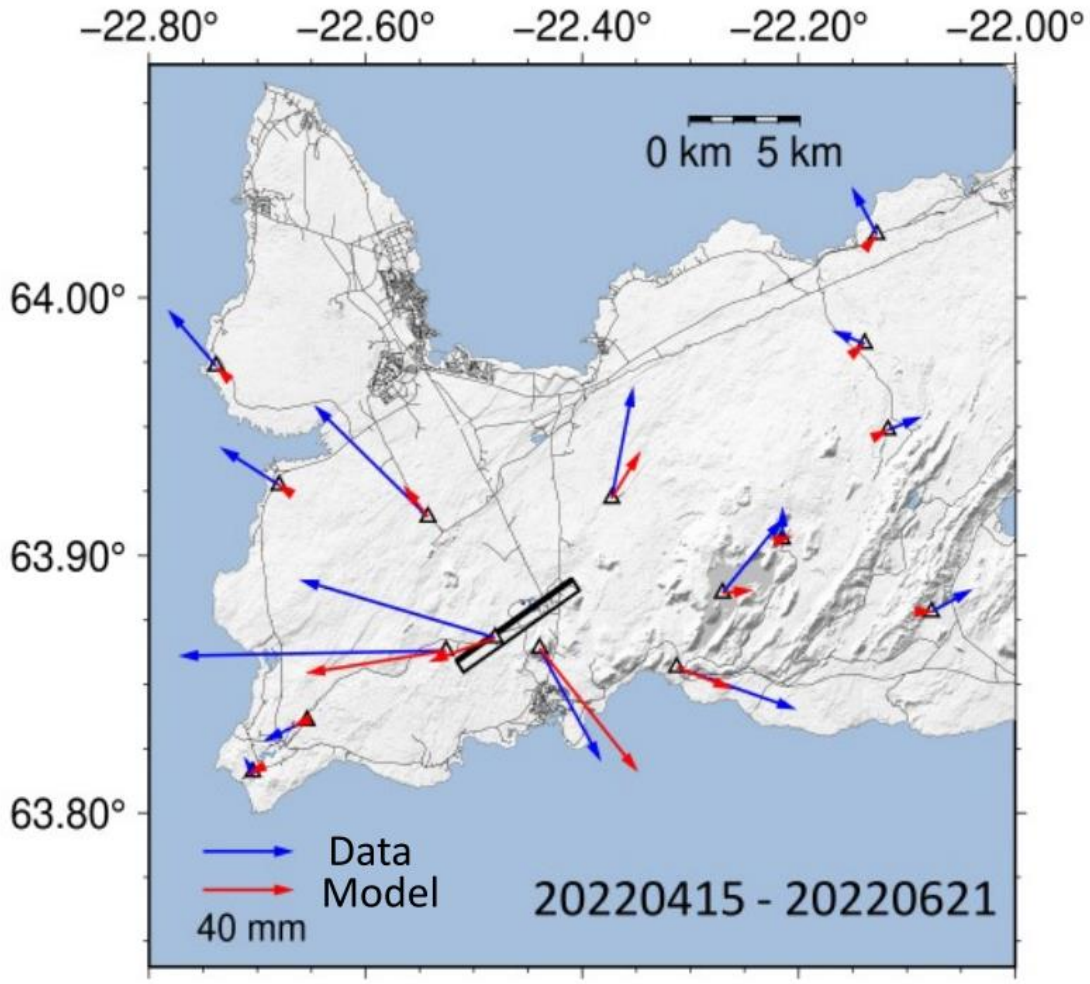

Fig. S18.
Uplift period at Svartsengi April 15 – June 21, 2022. Predicted displacements for a best fitting sill model and observations are compared. GNSS horizonal displacements are indicated by blue arrows and the model predictions are indicated by red arrows. The thicker black line indicates the inferred surface projection of the sill at surface, while the thinner indicates the projection of the bottom part of the sill.

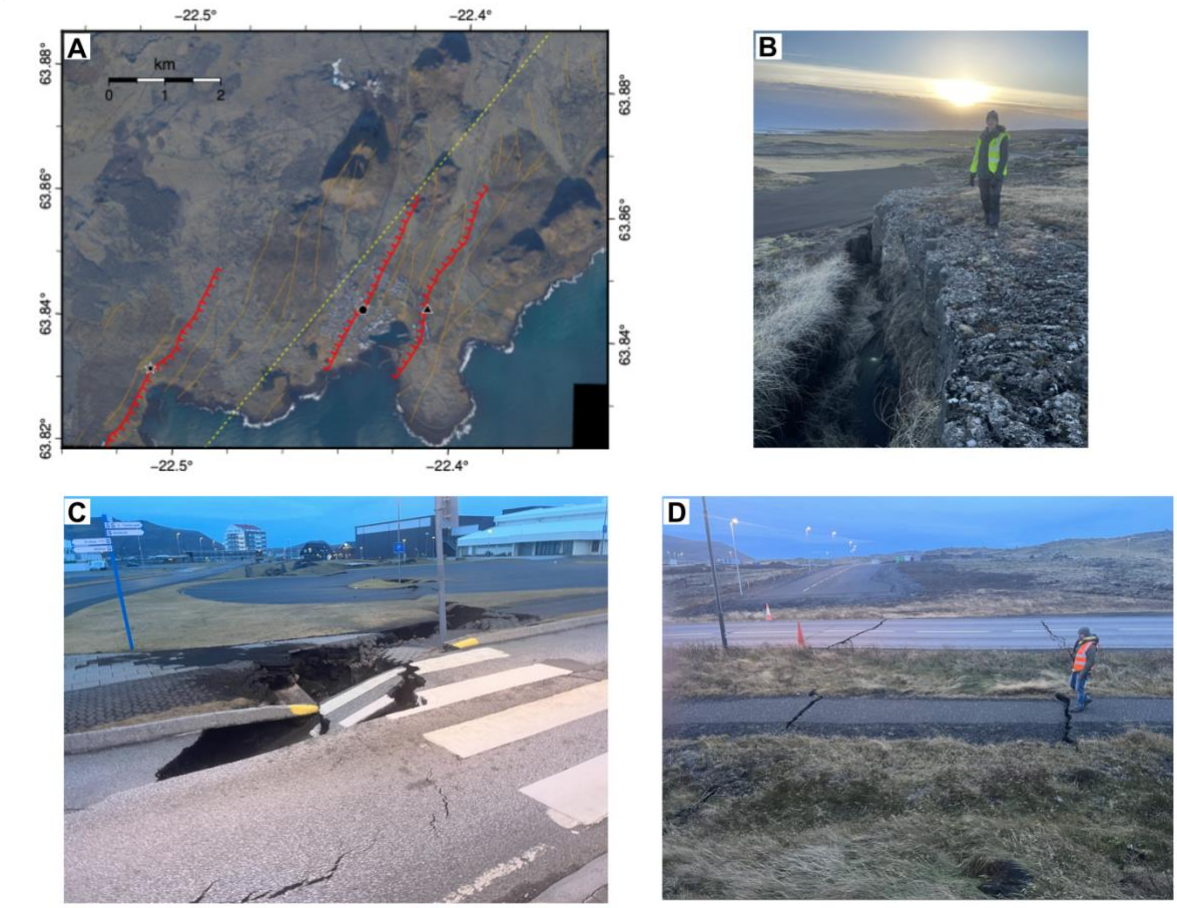

Fig. S19.
Graben map with large normal faults (red comb line) and other faults (orange line) activated during the dike propagation and the following days. Photo locations are indicated with star (panel B), circle (panel C) and triangle (D). Approximate dike location is indicated with yellow dashed line). Background shows an aerial orthoimage acquired on November 2, 2023 (collected and processed by Náttúrufræðistofnun Íslands & Landmælingar Íslands).

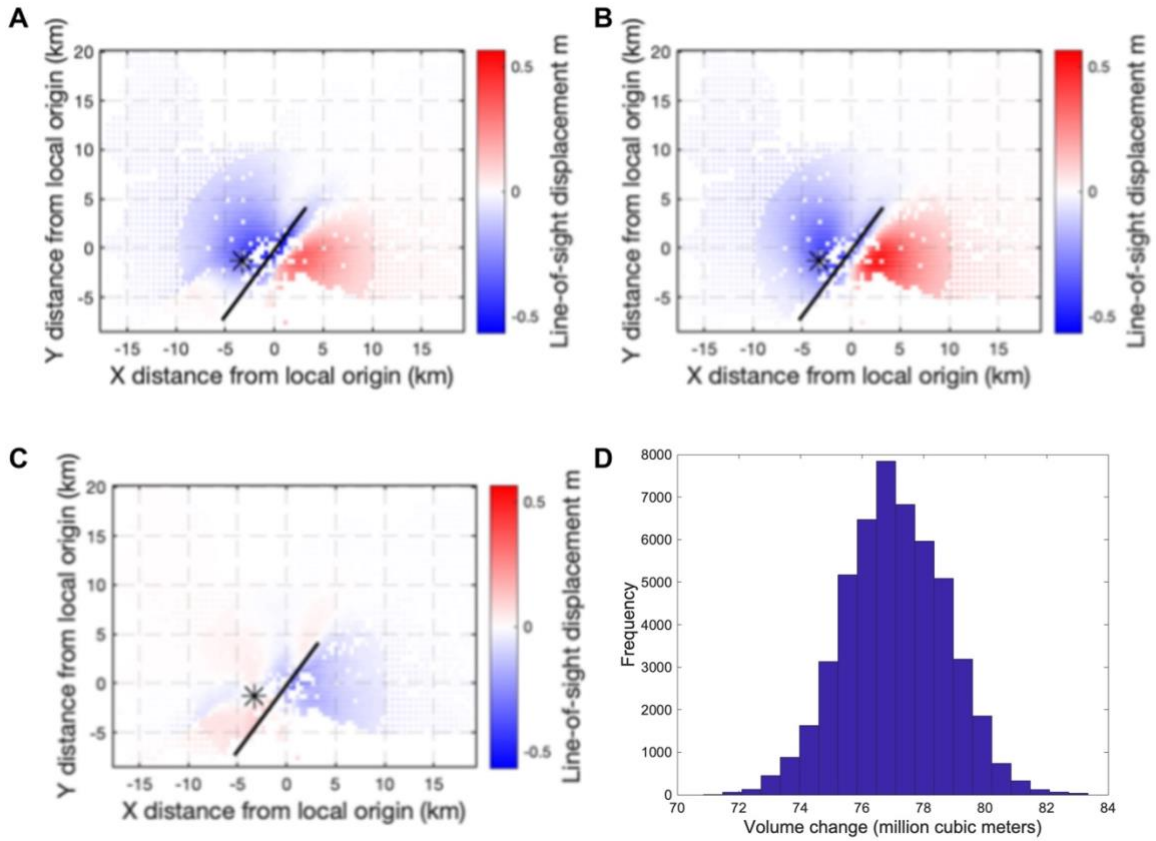

Fig. S20.
First dike model (for November 10, up until 19:35 UTC) with observation (A), model prediction (B), and residuals (C). Unscaled probability density function of dike volume is displayed in panel D.

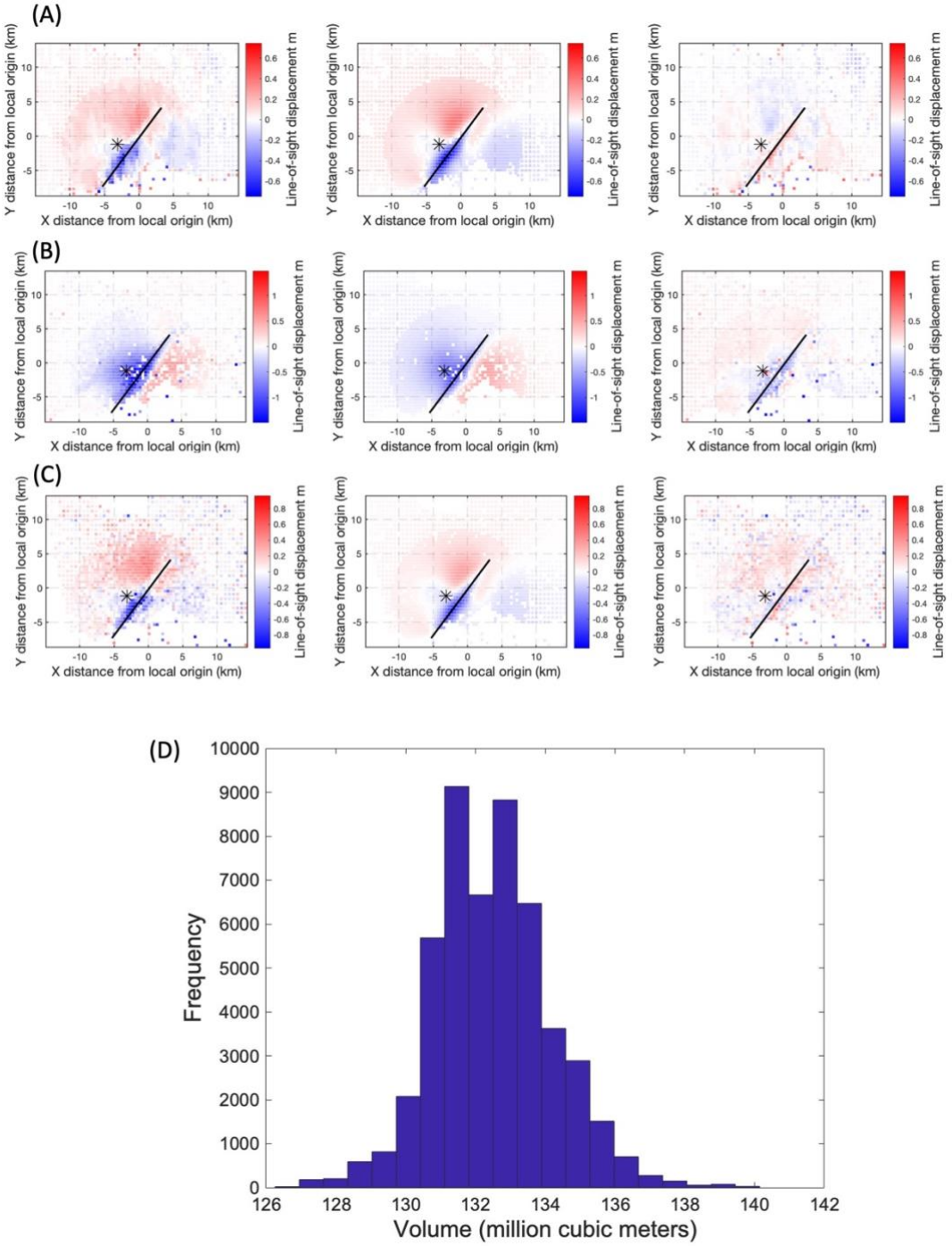

Fig. S21.
Dike model for November 10 – 12 with observations (left sub-panels), model predictions (middle sub-panels), and residuals (right sub-panels) for Sentinel-1 (A), ICEYE (B), CSK (C). Unscaled probability density function of dike volume is displayed in panel D.

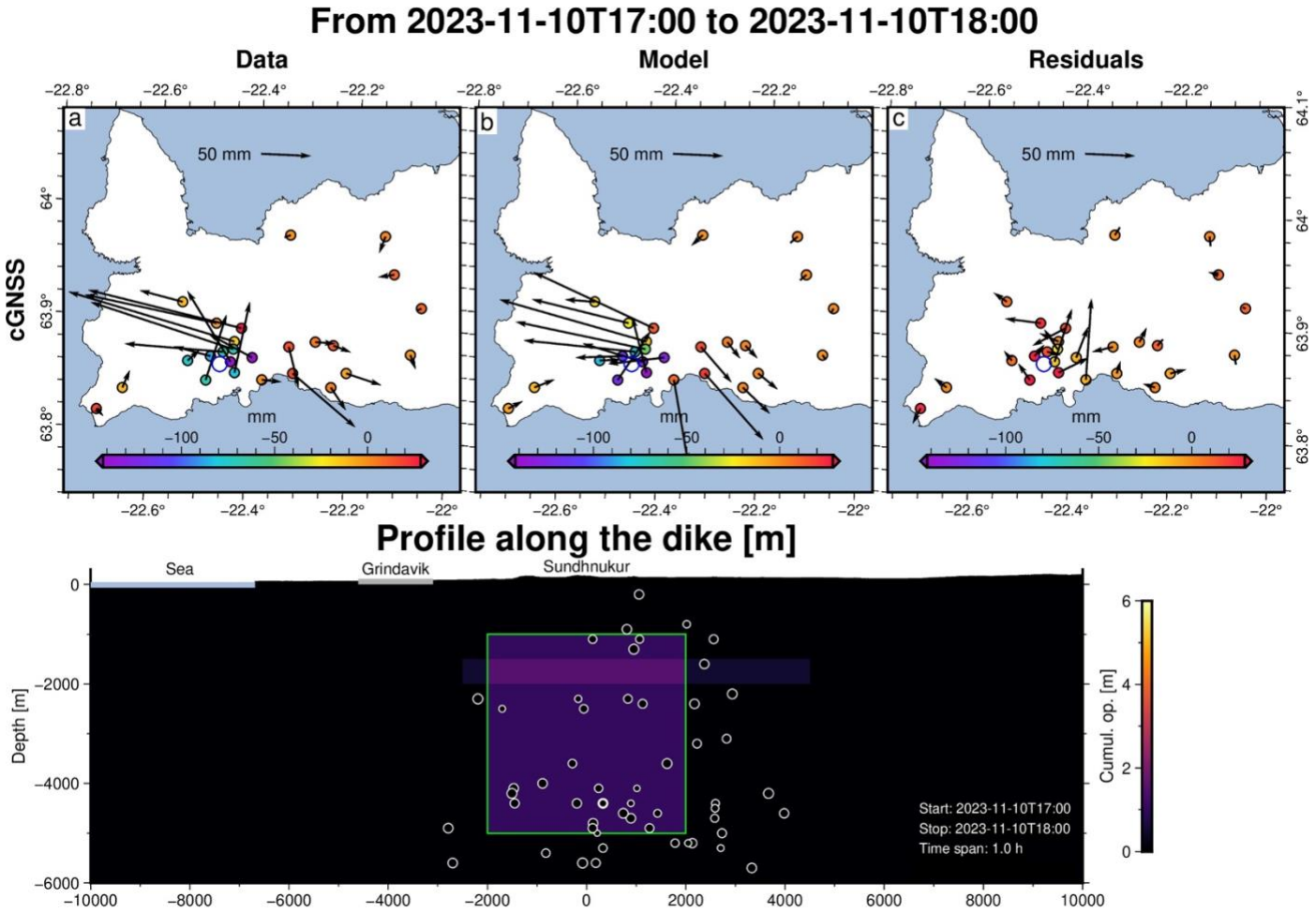

Fig. S22.
Hourly dike model from GNSS observations during the 10-12 November 2023 diking event. Example of observations, model, residuals and inferred dike opening. Time period from 17:00 – 18:00 on November 10, 2023.

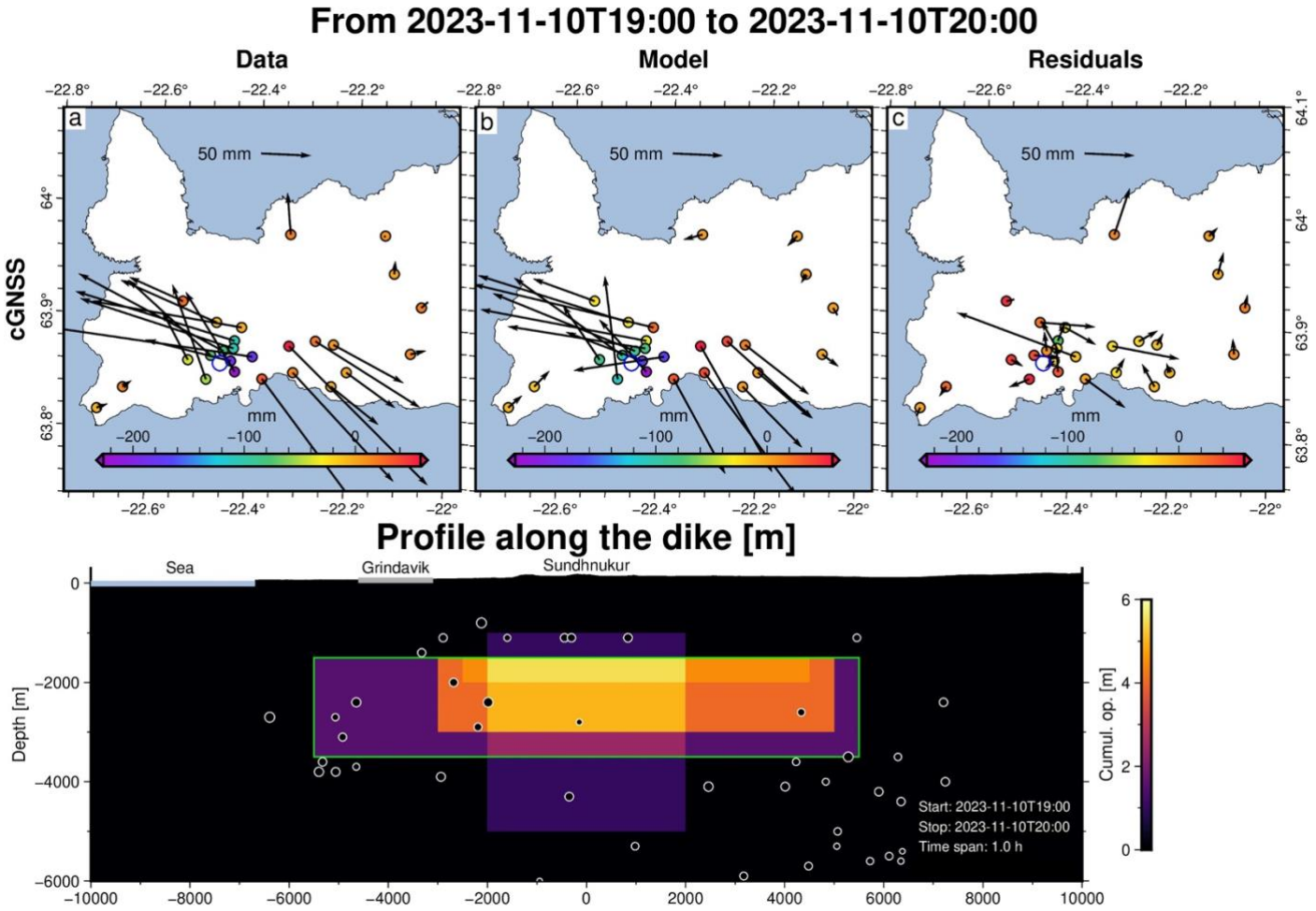

Fig. S23.
Hourly dike model from GNSS observations during the 10-12 November 2023 diking event. Example of observations, model, residuals and inferred dike opening. Time period from 19:00 – 20:00 on November 10, 2023. Note: maximum scaled inflow rate to dike during this period is 7400 m^3/s.

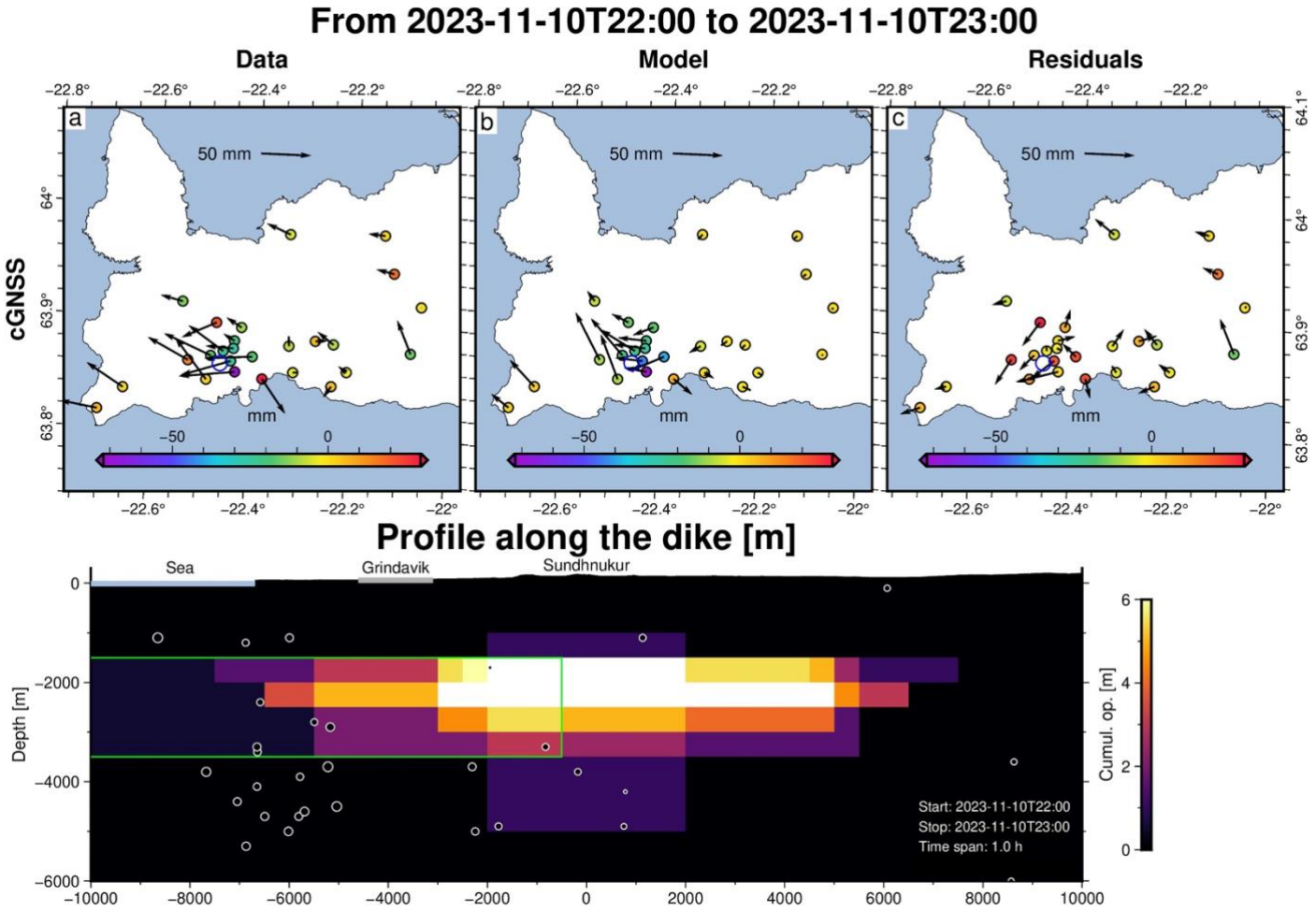

Fig. S24.
Hourly dike model from GNSS observations during the 10-12 November 2023 diking event. Example of observations, model, residuals and inferred dike opening. Time period from 22:00 – 23:00 on November 10, 2023.

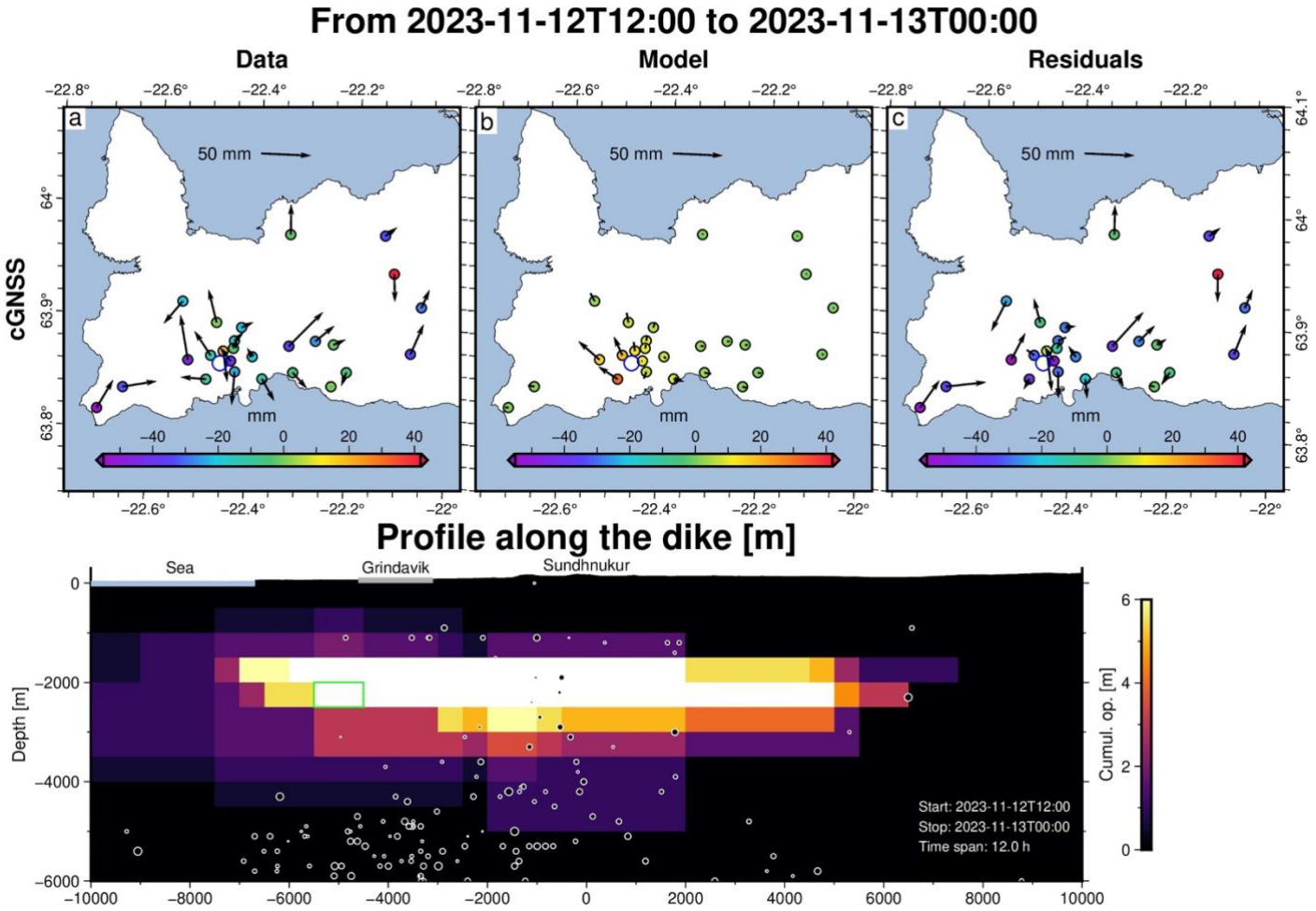

Fig. S25.
Hourly dike model from GNSS observations during the 10-12 November 2023 diking event. Example of observations, model, residuals and inferred dike opening. Time period from 12:00 on November 12 – 00:00 on November 13, 2023.

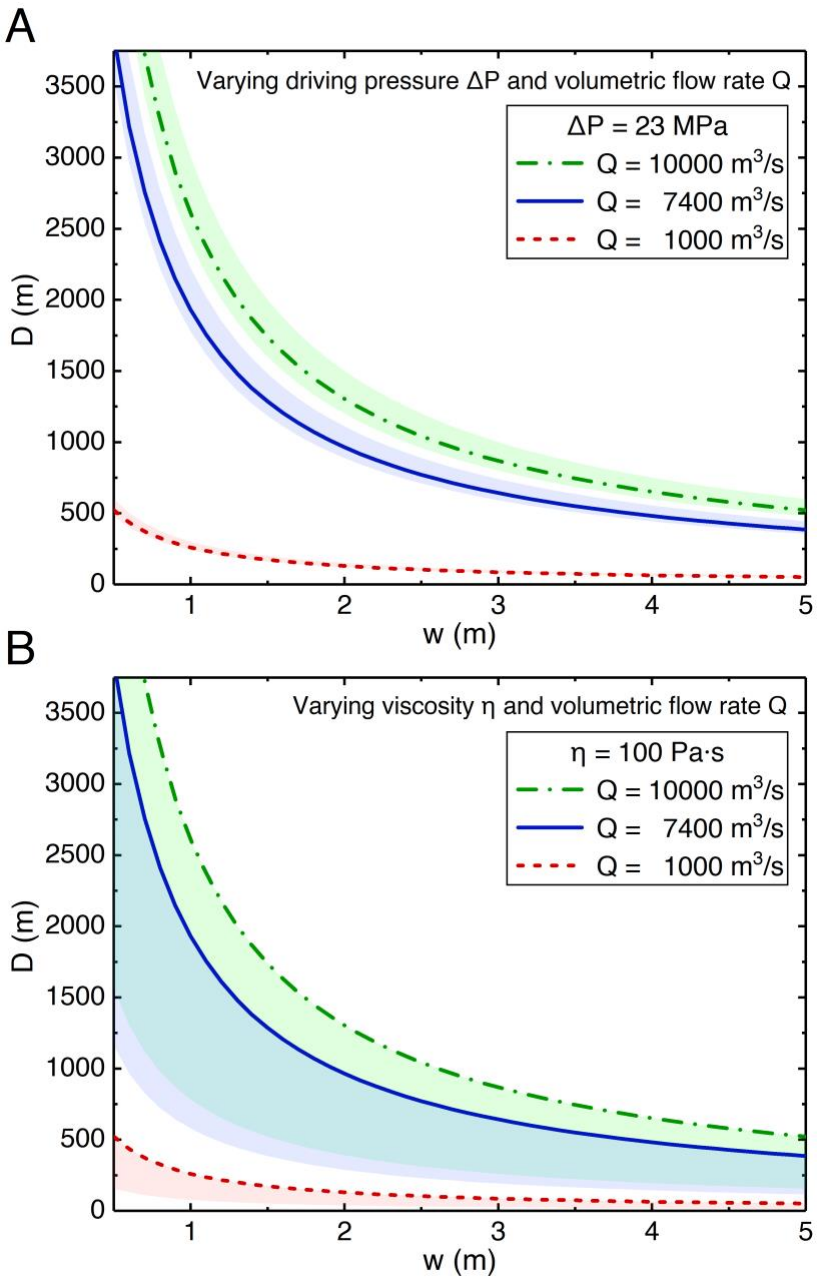

Fig. S26.
The relationship between the short (*w*) and long side (*D*) of the cross-sectional area of the dike with a channel length of 5 km based on equations (1) and (2). Different colors and styles of lines indicate different volumetric flow rates. (A) The shaded areas show the range of *D* with driving pressure (*ΔP*) between 20 MPa (upper edges) and 25 MPa (lower edges). The lines assume *ΔP* being 23 MPa. (B) The shaded areas show the range of D with viscosity between 10 Pa s (lower edges) and 100 Pa s (upper edges). The maximum volumetric flow rate inferred from geodetic modelling was ~ 7400 m^3/s, but significantly lower during a large part of the main opening phase of the dike (Fig. 5).

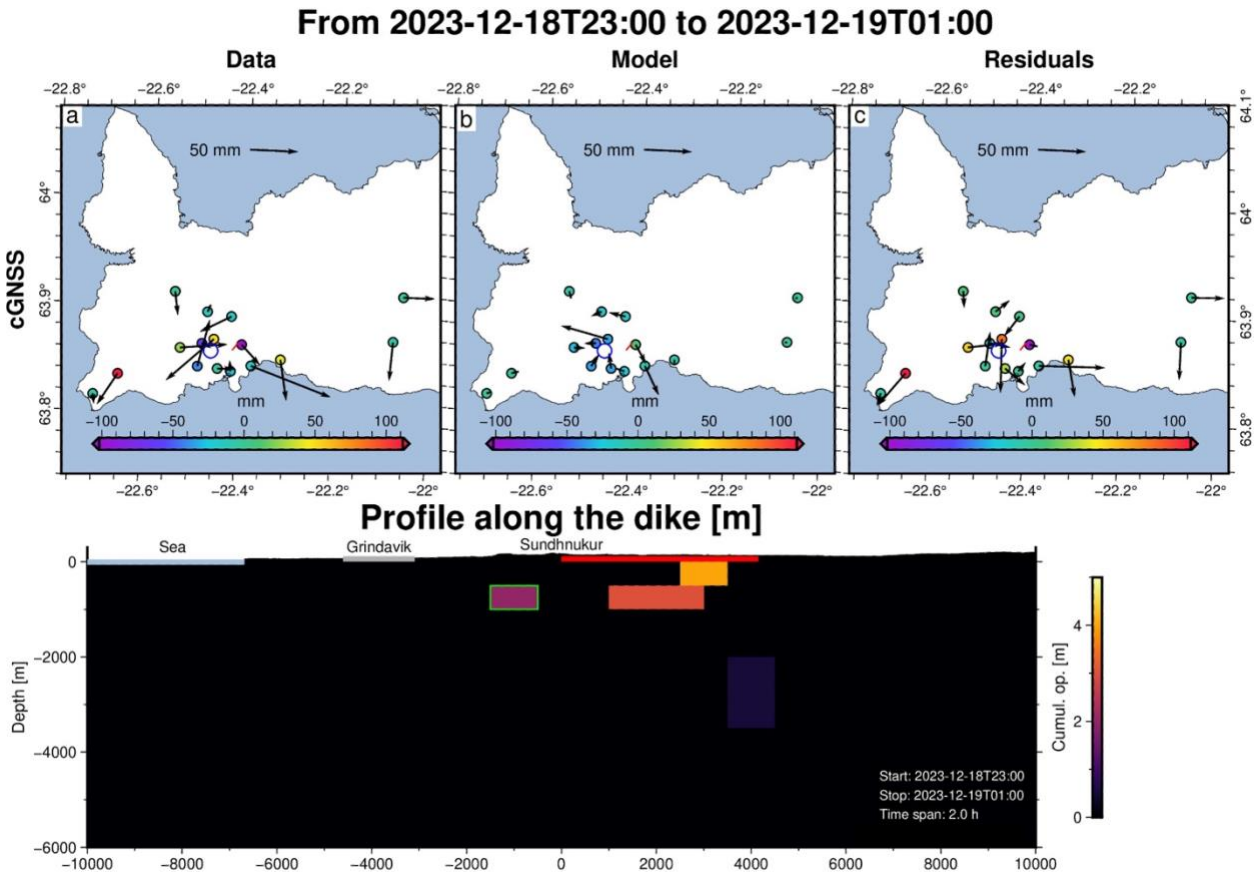

Fig. S27.
Hourly dike model from GNSS observations during the 18-21 December 2023 diking and eruption. Example of observations, model, residuals and inferred dike opening. Time period from 23:00 on December 18 – 01:00 on December 19, 2023. Peak inflow into the dike: ~800 m^3/s (18 Dec. 22:00-23:00).

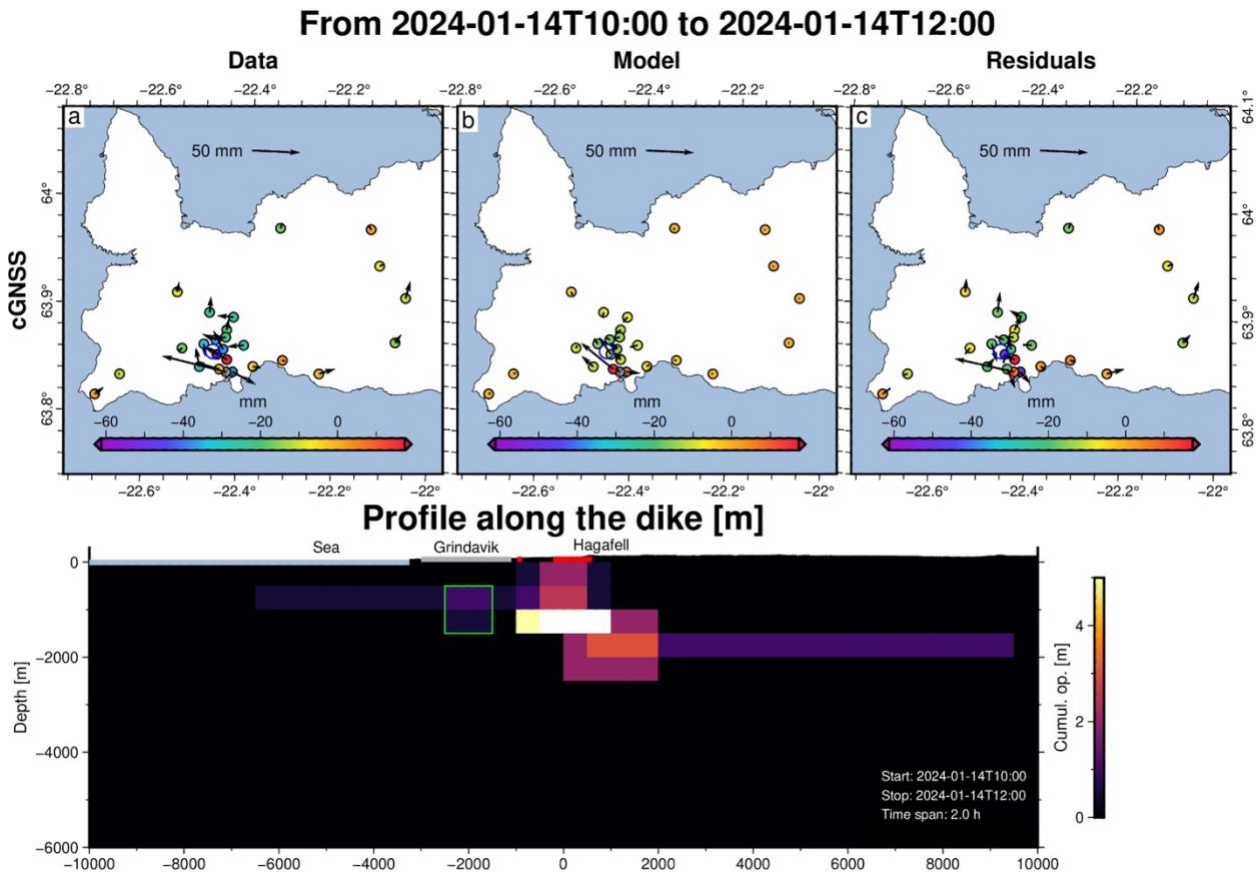

Fig. S28.
Hourly dike model from GNSS observations during the 14-16 January 2024 diking and eruption. Example of observations, model, residuals and inferred dike opening. Time period from 10:00 – 12:00 on January 14, 2024. Peak inflow into the dike: ~1700 m^3/s (14 Jan. 04:00-05:00).

Additional references

59. F. Lyard, F. Lefevre, T. Letellier, O. Francis, Modelling the global ocean tides: modern insights from FES2004. *Ocean Dyn.* **56**, 394–415 (2006).

60. J. F. Zumberge, M. B. Heflin, D. C. Jefferson, M. M. Watkins, F. H. Webb, Precise point positioning for the efficient and robust analysis of GPS data from large networks. *J. Geophys. Res. Solid Earth* **102**(B3), 5005–5017 (1997).

61. T. A. Herring, R. W. King, M. A. Floyd, S. C. McClusky, GAMIT reference manual: GPS analysis at MIT release 10.7 (Massachusetts Institute of Technology, 2018); http://geoweb.mit.edu/gg/GAMIT_Ref.pdf.

62. W. Bertiger, S. D. Desai, B. Haines, N. Harvey, A. W. Moore, S. Owen, J. P. Weiss, Single receiver phase ambiguity resolution with GPS data. *J. Geod.* **84**, 327–337 (2010).

63. T. Takasu, RTKLIB: Open Source Program Package for RTK-GPS in *Proceedings of the international conference for Free and Open Source Software for Geospatial*, Tokyo, Japan, 2 November 2009.

64. P. A. Rosen, E. Gurrola, G. F. Sacco, H. Zebker, The InSAR scientific computing environment, in *Proceedings of 9th European Conference on Synthetic Aperture Radar* (EUSAR, 2021), pp. 730–733.

65. C. W. Chen, H. A. Zebker, Network approaches to two-dimensional phase unwrapping: intractability and two new algorithms. *J. Opt. Soc. Am. B.* **17**, 401–414 (2000).

66. R. Böðvarsson, S. T. Rögnvaldsson, R. Slunga, E. Kjartansson, The SIL data 323 acquisition at present and beyond year 2000. *Phys. Earth Planet. Inter.* **113**, 89–101 (1999).

67. S. S. Jakobsdóttir, Seismicity in Iceland: 1994–2007. *Jökull* **58**, 75–100 (2008).

68. R. Slunga, S. T. Rögnvaldsson, R. Böðvarsson, Absolute and relative locations of similar events with application to microearthquakes in southern Iceland. *Geophys. J. Int.* **123**, 409–419 (1995).

69. F. Sigmundsson, A. Hooper, S. Hreinsdóttir, K. S. Vogfjörd, B. G. Ófeigsson, E. R. Heimisson, S. Dumont, M, Parks, K. Spaans, G. B. Gudmundsson, V. Drouin, T. Árnadóttir, K. Jónsdóttir, M. T. Gudmundsson, T. Högnadóttir, H. M. Fridriksdóttir, M. Hensch, P. Einarsson, E. Magnússon, S. Samsonov, B. Brandsdóttir, R. S. White, T. Ágústsdóttir, T. Greenfield, R. G. Green, Á. R. Hjartardóttir, R. Pedersen, R. A. Bennett, H. Gerirsson, P. C. La Femina, H. Björnsson, F. Pálsson, E. Sturkell, C. J. Bean, M. Möllhoff, A. K. Braiden, E. P. S. Eibl, Segmented lateral dyke growth in a rifting event at Bárðarbunga volcanic system, Iceland. *Nature* **517**, 191–195 (2015).

70. S. Th. Rögnvaldsson and R Slunga. Routine fault-plane solutions for local networks: A test with synthetic data. *Bull. Seism. Soc. Am.* **83**, 1232–1247 (1993).

71. G. G. Pétursson and Kristín S. Vogfjörð. Attenuation relations for near- and farfield peak ground motion (PGV, PGA) and new magnitude estimates for large earthquakes in SW-Icelanfor Iceland. *Icelandic Meteorological Office report*, VÍ 2009-012, (2009). https://www.vedur.is/media/vedurstofan/utgafa/skyrslur/2009/VI_2009_012.pdf

72. M. Bagnardi, & A. Hooper, A., Inversion of surface deformation data for rapid estimates of source parameters and uncertainties: A Bayesian approach. *Geochemistry, Geophysics, Geosystems*, **19**, 2194–2211. (2018).